

Euler-Euler / RANS Modeling of Solid-liquid Flow in Stirred Tanks: a Comprehensive Model Validation

Shi, P.; Sommer, A.-E.; Rox, H.; Eckert, K.; Rzehak, R.;

Originally published:

June 2022

Minerals Engineering 185(2022), 107679

DOI: <https://doi.org/10.1016/j.mineng.2022.107679>

Perma-Link to Publication Repository of HZDR:

<https://www.hzdr.de/publications/Publ-34596>

Release of the secondary publication
on the basis of the German Copyright Law § 38 Section 4.

CC BY-NC-ND

1
2 Euler-Euler / RANS Modeling of Solid-liquid Flow in Stirred Tanks:
3 a Comprehensive Model Validation
4

5
6 Pengyu Shi^{1*}, Anna-Elisabeth Sommer¹, Hannes Rox¹, Kerstin Eckert^{1,2}, Roland Rzehak¹

7 ¹ Helmholtz-Zentrum Dresden – Rossendorf, Institute of Fluid Dynamics,
8 Bautzner Landstrasse 400, D-01328 Dresden, Germany

9 ² Technische Universität Dresden, Institute of Process Engineering and Environmental
10 Technology, D-01062 Dresden, Germany
11

12
13
14 **Abstract**
15

16 Simulations of solid-liquid flow on industrial scales are feasible within the Euler-Euler / RANS
17 approach. The reliability of this approach depends largely on the closure models applied to describe
18 the unresolved phenomena at the particle scale, in particular the interfacial forces. In this work, a
19 set of closure models [assembled previously for this kind of application](#) (Shi and Rzehak 2020) is
20 further validated by comparing the predictions to a recent experiment on stirred-tank flows (Sommer
21 et al. 2021), [which focuses on dilute suspensions](#). The dataset used for validation comprises 14
22 different experimental cases, covering a wide range of particle slip Reynolds number, impeller
23 Reynolds number, and particle Stokes number. For each case, simulation results on the solid velocity
24 and volume fraction as well as liquid velocity and turbulence are compared with the experimental
25 data. It turns out that by and large the experimental data are reasonably well reproduced. However,
26 the measurements show a small but clear effect of modulation of the liquid phase turbulence by the
27 particles. Therefore, several particle-induced turbulence (PIT) models based on the available
28 literature are assessed as well. Our results indicate a reduction in the predicted fluctuations by all
29 PIT models, which improves the results in cases with turbulence suppression but deteriorates those
30 with turbulence augmentation.
31

32 **Keywords:** stirred tanks, solid-liquid flow, Euler-Euler two-fluid model, Reynolds-stress turbulence
33 model, particle-induced turbulence

* Corresponding author email: p.shi@hzdr.de

34 1 INTRODUCTION

35 Stirred tank reactors are widely used in the minerals industry to maintain solids suspension in
36 continuous hydrometallurgical processes, such as leaching, oxidation, precipitation, neutralization
37 and storage (Wu et al. 2015). For most of these operations, the process performance depends largely
38 on the homogeneity of the suspension, which in turn depends on the fluid and solid dynamics, in
39 particular the turbulence in the liquid phase. Moreover, understanding the two-phase dynamics in
40 solid-liquid stirred tanks and providing validated models are the preconditions for the modeling of
41 three phase (gas-solid-liquid) flow in flotation, which is a critical unit operation used to concentrate
42 valuable minerals in many mineral processing operations (Schwarz et al. 2019, Mesa and Brito-
43 Parada 2019). Therefore, quite a few research works on the dynamic behavior of solid-liquid
44 suspensions have been conducted in the past as reviewed in Mishra and Ein-Mozaffari (2020).

45 Computational fluid dynamics (CFD) simulations of solid-liquid two-phase flow in stirred tanks
46 are feasible within the Eulerian two-fluid framework of interpenetrating continua. However,
47 accurate numerical predictions rely on suitable closure models describing unresolved phenomena,
48 in particular the interfacial forces. As shown by the comprehensive literature review in Shi and
49 Rzehak (2020), a large number of works exist, in each of which largely a different and often
50 incomplete set of closure relations is compared to a different set of experimental data. For the
51 limited range of conditions to which each model variant is applied, reasonable agreement with the
52 data is mostly obtained, but due to a lack of comparability between the individual works no
53 complete, reliable, and robust formulation has emerged so far. Moreover, usually a number of
54 empirical parameters are involved and have been adjusted to match the particular data, which
55 deteriorates the model's applicability.

56 To make a first step towards a predictive model, we consider dilute suspensions ($0.01\% < \alpha_S \leq$
57 0.1%) where two-way coupling between the phases is necessary (Elghobashi 2006). Apart from
58 interest in its own right, results obtained for this restricted problem also provide a good starting
59 point for the investigation of more complex situations including flows with moderate to high solids
60 loading (Derksen 2018), heat and mass transport (Lu et al. 2019), or gas-solid-liquid three-phase
61 flows (Kim and Kang 1997).

62 Aspects requiring closure for the system under consideration are: (i) the momentum exchange
63 between the two phases, and (ii) the modulation of the turbulence of the liquid carrier phase by the
64 particles.

65 Regarding the first aspect, suitable closure relations therefor have previously been collected into a
66 baseline model that serves as a starting point for the simulation of such systems (Shi and Rzehak
67 2020). There, in addition to the baseline model which takes the full set of closure models (i.e. drag,
68 lift, virtual mass, and turbulent dispersion force) into consideration, seven reduced model variants
69 (summarized in Table 8 of Shi and Rzehak 2020) that originate from different combinations of
70 interfacial force correlations were considered to highlight the importance of various aspects. The
71 predictions were compared with the experimental data from Nouri and Whitelaw (1992), Montante
72 et al. (2012), and Tamburini et al. (2013) and the large-eddy-simulation results from Guha et al.
73 (2008). In most of these works inhomogeneous suspensions have been considered. According to
74 the comparisons, no simplifications were found to be possible in general. More specifically, 1)
75 often the agreement with the validation data deteriorates when using reduced models; 2) the choice
76 of models variants strongly affects the predictions for the solid fraction but only weakly affects
77 those for the mean and fluctuation velocities.

78 Expanding the range of validity of the baseline model is the major aim of this study, since only a
79 limited range of parameters was covered by the then available data used in Shi and Rzehak (2020).
80 In addition, none of these datasets comprised a full set of observables including solid velocity and
81 volume fraction as well as liquid velocity and turbulence. The recent experiment of Sommer et al.
82 (2021) provides all of these quantities at conditions with varying particle size, particle-to-liquid
83 density ratio, mean solid volume fraction, and impeller rotation speed. These new experimental
84 data now allow to conduct a more systematic validation of the closure models in the present work.

85 As for the second aspect, the liquid turbulence can be either suppressed or enhanced depending on
86 the detailed flow conditions. Possible mechanisms causing turbulence suppression comprise (Eaton
87 2009; Balachandar and Eaton 2010) (a) the enhanced inertia of the particle-laden flow, (b) the
88 enhanced effective viscosity of the particle-laden fluid, and (c) the increased dissipation arising
89 from particle drag. On the other hand, particles may also enhance the turbulence via the two
90 mechanisms: (d) the enhanced velocity fluctuation due to wake dynamics and (e) buoyancy-
91 induced instabilities due to density variation arising from preferential particle concentration. In
92 practice, enhancement and suppression take place simultaneously and the overall modulation
93 depends on the relative strength of the different mechanisms (Elghobashi and Truesdell 1993;
94 Druzhinin and Elghobashi 1999; Balachandar and Eaton 2010, Mathai et al. 2020).

95 Different criteria to distinguish the enhancement or the suppression effects have appeared in the
96 past. The probably most widely known one originates from Gore and Crowe (1989), according to
97 which particles suppress (enhance) the liquid turbulence when the particle size is smaller (larger)
98 than the characteristic size of large eddies. This classification does not comprise the effects of
99 changing particle material density, nor does it capture the effects of other important parameters
100 such as the Stokes number (Eaton and Fessler 1994; Ferrante and Elghobashi 2003), which relates
101 to mechanisms (c) and (e), or the particle Reynolds number (Hetsroni 1989; Hoque et al. 2016),
102 which relates to mechanisms (c) and (d). Recent efforts have sought new criteria to collapse
103 turbulence modulation data. New dimensionless parameters e.g. Stokes load (Poelma et al. 2007)
104 and particle momentum number (Tanaka and Eaton 2008) have therefore been proposed based on
105 more rigorous physical arguments. Nevertheless, a comprehensive assessment carried out by Gai
106 et al. (2020) has indicated that the turbulence modulation cannot be fully characterized by a single
107 parameter. Hence, a reliable model is still not available even for highly simplified situations, e.g.
108 for particles in homogeneous and isotropic turbulence (Meyer 2012, Gai et al. 2020).

109 Previous E-E simulations of particle-laden stirred-tank flows have therefore either neglected the
110 effect all together or employed highly simplified phenomenological models (see the review in Shi
111 and Rzehak 2020). These models are generally based on two different approaches. The first
112 originates from Sato et al (1981) and treats the particle effects as an additional term in the effective
113 liquid viscosity. Obviously, this approach always predicts an increase in turbulent viscosity
114 (Ochieng and Onyango 2008, Murthy et al. 2008, Qi et al. 2013). The second approach is to add
115 source terms directly to the generation terms in the turbulence model equations following Kataoka
116 et al. (1992). Since both the turbulent kinetic energy and dissipation (or other equivalent parameters
117 e.g. eddy frequency) are modified, this approach can in principle both increase or decrease the
118 turbulent viscosity. Prior work applying this approach may be found in Wang et al. (2003), Shan
119 et al. (2008), and Feng et al. (2012). The performance of these two different approaches has not yet
120 been assessed systematically for particle-laden flows, but they have been verified extensively in
121 bubbly flow simulations (see Rzehak and Krepper (2013) for a review).

122 That the turbulence modulation by rigid particles and by bubbles can be modeled in an analogous
123 way is not surprising. In particular, it has been shown in the experiments summarized by Gore and
124 Crowe (1989) and newer ones conducted by Hosokawa and Tomiyama (2004) that the turbulence
125 modulation may be described in a unified manner irrespective of the nature of the disperse phase.
126 This similar behavior may be understood by the following two mechanisms. For relatively large
127 particles the wake dynamics is known to be governed by many-body interactions, which act
128 similarly for solid spheres and bubbles (Risso 2008). On the other hand, for small-but-finite-size
129 particles, the modulation of the spectra of both the turbulent kinetic energy and the dissipation has
130 been shown (Yeo et al. 2010) to be closely correlated with the size of the particles but not their
131 inertia. Recent works (Santarelli and Fröhlich 2015, 2016; Yu et al. 2021, Xia et al. 2021) have
132 highlighted the anisotropic nature of the turbulence modulation. Advanced models accounting for
133 this effect have already been proposed for bubbly flows (Colombo and Fairweather 2015; Parekh
134 and Rzehak 2018; Ma et al. 2020), in combination with RSM turbulence models. The applicability
135 of such advanced PIT models, as well as those based on the two common approaches above, will
136 be assessed here for particle-laden flow in stirred tanks.

137 The remainder of the paper proceeds as follows. In the next section, the E-E /RANS approach
138 together with all investigated PIT models are summarized. Full details of the baseline model from
139 (Shi and Rzehak 2020) are provided for convenience in the Supplementary Material. In section 3,
140 first the selected test cases from the experiment of Sommer et al. (2021) and the numerical setup
141 are outlined, details of the latter being relegated to the Supplementary Material. Then, the
142 simulation results are discussed considering first a base case and then the effect of parametric
143 variations. Lastly an assessment of different PIT model is given. A final summary and conclusions
144 are provided in section 4.

145

146 2 OVERVIEW OF MODELS

147 This section summarizes the models used in the present work. Section 2.1 introduces the
148 conservation equations of the E-E framework and the model used in modeling the turbulence in the
149 liquid phase. The various models on the particle-induced turbulence are described in section 2.2.

150 2.1 Euler-Euler / RANS approach

151 The conservation of mass in the solid and liquid phases is governed by the continuity equation

$$\frac{\partial}{\partial t}(\alpha_k \rho_k) + \nabla \cdot (\alpha_k \rho_k \mathbf{u}_k) = 0 \quad (1)$$

152 with the index $k = L, S$ denoting the liquid and solid phases, respectively. In Eq. (1), α is the
153 volume fraction, ρ denotes the density, \mathbf{u} is the phase-weighted mean velocity (Drew and Passman,
154 2006).

155 The motion of the two phases is governed by the Naiver-Stokes equation, which, in the E-E
156 framework, takes the form

$$\begin{aligned} \frac{\partial}{\partial t}(\alpha_k \rho_k \mathbf{u}_k) + \nabla \cdot (\alpha_k \rho_k \mathbf{u}_k \otimes \mathbf{u}_k) = \\ -\alpha_k \nabla p_k + \nabla \cdot (2\alpha_k \mu_k^{\text{mol}} \mathbf{D}_k) - \nabla \cdot (\alpha_k \rho_k \mathbf{R}_k) + \mathbf{F}_k^{\text{body}} + \mathbf{F}_k^{\text{inter}}. \end{aligned} \quad (2)$$

157 Here p denotes the pressure, $\mathbf{D} = (\nabla\mathbf{u} + (\nabla\mathbf{u})^T)/2$ is the strain rate tensor, and μ^{mol} is the
 158 molecular dynamic viscosity. Following previous numerical work, μ_S^{mol} is assumed to be identical
 159 with μ_L^{mol} .

160 The body forces $\mathbf{F}_k^{\text{body}}$ comprise the gravity force as well as centrifugal and Coriolis forces where
 161 a rotating frame of reference is adopted. The term $\mathbf{F}_k^{\text{inter}}$ accounts for the momentum transfer
 162 between the phases. Due to momentum conservation the relation $\mathbf{F}_S^{\text{inter}} = -\mathbf{F}_L^{\text{inter}}$ holds. This term
 163 comprises of a number of contributions and the corresponding models employed here are
 164 summarized in Table 1. [A detailed discussion thereof is given in section A of the Supplementary](#)
 165 [Material](#).

166 Table 1: Summary of particle force correlations [based on two-way coupling](#).

force	reference
drag	Schiller and Naumann (1933) modified for turbulence effects as in Shi and Rzehak (2020)
lift	Shi and Rzehak (2019)
turbulent dispersion	Lopez de Bertodano (1998) with turbulence time scales from Shi and Rzehak (2020)
virtual mass	constant coefficient $C_{\text{VM}} = 1/2$

167
 168 In Eq. (2), \mathbf{R} is the Reynolds stress tensor and is defined in terms of the turbulent fluctuating
 169 velocities \mathbf{u}'_k as $\mathbf{R}_k = \langle \mathbf{u}'_k \otimes \mathbf{u}'_k \rangle$, where $\langle \ \rangle$ corresponds to ensemble averaging. \mathbf{R}_L is obtained
 170 by directly solving a transport equation as discussed in the following, while \mathbf{R}_S is presently
 171 neglected. The index ‘L’ is then dropped throughout this section for notational convenience. The
 172 transport equation for the Reynolds stress tensor $\mathbf{R} = \langle \mathbf{u}' \otimes \mathbf{u}' \rangle$ is given as

$$\begin{aligned} \frac{\partial}{\partial t}(\alpha\rho\mathbf{R}) + \nabla \cdot (\alpha\rho\mathbf{u} \otimes \mathbf{R}) &= \nabla \cdot (\alpha(\boldsymbol{\mu}^{\text{mol}} + C_s\boldsymbol{\mu}^{\text{turb}})\nabla \otimes \mathbf{R}) \\ &+ \alpha\rho \left(\mathbf{P} + \boldsymbol{\Phi} - \frac{2}{3}\varepsilon\mathbf{I} + \mathbf{G} \right) + \mathbf{S}^R, \end{aligned} \quad (3)$$

173 and that for the isotropic turbulent dissipation rate ε as

$$\begin{aligned} \frac{\partial}{\partial t}(\alpha\rho\varepsilon) + \nabla \cdot (\alpha\rho\mathbf{u}\varepsilon) &= \nabla \cdot (\alpha(\boldsymbol{\mu}^{\text{mol}} + C_\varepsilon\boldsymbol{\mu}^{\text{turb}}) \cdot \nabla\varepsilon) \\ &+ \alpha\rho \frac{\varepsilon}{k} \left(C_{\varepsilon,1} \frac{1}{2} \text{tr}(\mathbf{P}) - C_{\varepsilon,2}\varepsilon \right) + S^\varepsilon. \end{aligned} \quad (4)$$

174 Individual terms appearing on the right side of equation (3) describe diffusion, production,
 175 pressure-strain correlation, dissipation, and generation due to body forces (here frame rotation).
 176 The last term in Eqs. (3) and (4), i.e. \mathbf{S}^R and S^ε , are the PIT source terms and will be described in
 177 section 2.2. The SSG RSM turbulence model proposed by Speziale, Sarkar, and Gatski (1991) is
 178 applied. A detailed description on the concept of this model as well as a summary on the values of
 179 the pertinent coefficients used in the present work can be found in Shi and Rzehak (2020).

180 2.2 Models for the particle-induced turbulence

181 In addition to the shear-induced turbulence discussed above, the presence of the particles induces
 182 additional disturbances to the ambient flow, which can either enhance or attenuate the turbulence
 183 depending on the flow condition. This turbulence modulation, also referred to as particle-induced

184 turbulence (PIT), needs to be modeled. In this context, a simple approach is to just add an extra
 185 particle-induced contribution to the effective viscosity following Sato et al (1981, hereafter termed
 186 Sato-PIT). Since the shear-induced turbulence here is modeled without referring to a turbulent
 187 viscosity, this approach is implemented by replacing the molecular viscosity of the liquid phase,
 188 μ_L^{mol} , in the momentum equation (2) by an effective viscosity

$$\mu_L^{\text{eff}} = \mu^{\text{mol}} + \mu^{\text{PIT}}, \quad (5)$$

189 where μ^{PIT} is the particle-induced contribution. Following Sato et al (1981), μ^{PIT} is modeled as

$$\mu^{\text{PIT}} = C_p \rho_L \alpha_S d_p u_{\text{rel}}, \quad (6)$$

190 where in accordance with previous works (Ochieng and Onyango 2008, Murthy et al. 2008, Qi et
 191 al. 2013) $C_p = 0.6$ is applied.

192 An alternative approach is to add source terms directly to the generation terms in the turbulence
 193 model equations following Kataoka et al. (1992). This approach may be implemented by
 194 expressing the source terms \mathbf{S}^R and S^ε in Eqs. (3) & (4) as

$$\mathbf{S}^R = S^k \left(a [\hat{\mathbf{u}}_{\text{rel}} \otimes \hat{\mathbf{u}}_{\text{rel}}] + \frac{1}{2} (2 - a) [\mathbf{I} - \hat{\mathbf{u}}_{\text{rel}} \otimes \hat{\mathbf{u}}_{\text{rel}}] \right) \quad (7)$$

195 and

$$S^\varepsilon = C_{\varepsilon P} \frac{S^k}{\tau}, \quad (8)$$

196 where S^k is proportional to the work due to the drag force, i.e.

$$S^k = C_{kP} \mathbf{F}_L^{\text{drag}} \cdot \mathbf{u}_{\text{rel}}. \quad (9)$$

197 In Eq. (7), \mathbf{I} is the identity matrix, $\hat{\mathbf{u}}_{\text{rel}}$ is a normalized vector in the direction of the relative
 198 velocity between the two phases, i.e. $\hat{\mathbf{u}}_{\text{rel}} = \mathbf{u}_{\text{rel}}/u_{\text{rel}}$. The two terms in the bracket of Eq. (7)
 199 correspond to the longitudinal and the transverse components of the contribution to the liquid
 200 Reynolds stress by the dispersed phase and the coefficient a governs their ratio.

201 The PIT model following this approach can assume two different forms depending on the value of
 202 the coefficient a appearing in Eq. (7). Assuming this contribution to be isotropic yields $a = 2/3$,
 203 which recovers the PIT model applied in prior works employing the isotropic two-equation
 204 turbulence models (e.g. Wang et al. 2003, Shan et al. 2008, and Feng et al. 2012). In these previous
 205 works the empirical coefficients $C_{\varepsilon P}$, C_{kP} appearing in Eqs. (8) and (9) were treated as small
 206 constants while the timescale τ in Eq. (8) was assumed to be proportional to k/ε . In the present
 207 work, the suggested correlations from Ma et al. (2017) are applied, which give

$$C_{\varepsilon P} = 0.3 C_{D,0}, \quad C_{kP} = \min(0.18 Re_p^{0.23}, 1), \quad \tau = d_p/u_{\text{rel}}. \quad (10)$$

208 Hereafter, the PIT model implemented following Eqs. (7)-(10) and $a = 2/3$ will be termed as
 209 iso-PIT.

210 Taking advantage of the SSG RSM model applied in this work, the source term \mathbf{S}^R can also be
 211 treated as anisotropic, which is indeed the case observed in both experimental (Geiss et al. 2004,
 212 Poelma et al. 2007) and DNS studies (Yu et al. 2021, Xia et al. 2021). Following Ma et al. (2020),
 213 a is correlated with the particle Reynolds number via

$$a = \min(0.67 + 0.67 \exp(370Re_p^{-1.2}), 2). \quad (11)$$

214 The PIT model implemented following Eqs. (7)-(11) will be termed as aniso-PIT.

215 The proposal to cast the source term \mathbf{S}^R following Eq. (7) deserves some explanation. First, it has
 216 to be pointed out that for flows in simple geometry, e.g. vertical pipe or channel flows, no such
 217 complexity is required, as the relative velocity is everywhere unidirectional and independent of
 218 position. The need to consider local variations of the direction of relative velocity arises when the
 219 flow considered is multi-dimensional, e.g. stirred-tank flows. In this case one has to cast the source
 220 term so that it is independent of the choice of coordinate directions. This can be proceed using the
 221 idea based on proper Euler angles (see Appendix C of Ma et al. (2020) for the details). After some
 222 manipulations, the transformation turns out to follow Eq. (7).

223

224 3 RESULTS AND DISCUSSION

225 The experiment of Sommer et al. (2021) investigated the solid-liquid two-phase flow in a stirred
 226 tank of a standard configuration. The tank was cylindrical and had a diameter $D_t = 90$ mm. The
 227 liquid fill height H was the same as the tank diameter, i.e. $H = 90$ mm. A standard Rushton turbine
 228 with a diameter $D_i = 30$ mm was installed with a separation distance from the tank bottom of $C_i =$
 229 30 mm. The height (axial) and width (radial) of the impeller blades are $H_{bla} = 6$ mm and $W_{bla} =$
 230 7.5 mm, respectively. Four baffles were installed on the tank wall every 90° , which extended over
 231 the entire tank height and had a width of 9 mm. Other geometric details can be found in Sommer
 232 et al. (2021). Deionized water was used as the liquid phase. Two different types of particles were
 233 considered, namely Polyethylene spheres (PE) and glass beads (GL) having a density ratio with
 234 respect to water of 1.1 and 2.5 , respectively. For each type of particles, different operational
 235 conditions concerning the impeller rotation speed Ω , the mean solid volume fraction $\bar{\alpha}_{S,ave}$, and
 236 the particle diameter d_p were considered in the experiment. 35 datasets comprising spatially
 237 resolved data on the solid mean velocity and solid fraction as well as liquid mean velocity and
 238 fluctuation are available from this experiment.

239 In the present work, CFD simulations are performed on 14 out of the 35 experimental cases. As
 240 summarized in Table 2, the investigated cases comprise one single-phase case with an impeller
 241 rotation speed of $\Omega = 1500$ rpm and two series of cases concerning two-phase flows which are
 242 distinguished by the type of the particle. For both the PE and GL series, the “base” case corresponds
 243 to the situation with $\Omega = 1500$ rpm, $\bar{\alpha}_{S,ave} = 0.05\%$, and $d_p = 0.165$ mm. In comparison, “vofS”
 244 and “vofL” correspond to cases with smaller and larger solid volume fractions of $\bar{\alpha}_{S,ave} = 0.025\%$
 245 and 0.1% , respectively. Similarly, cases involving relatively small (resp. large) particles are termed
 246 as “dpS” (resp. “dpL”), while those involving very small (resp. only moderate) values of impeller
 247 rotation speed are termed as “rpm650” (resp. “rpm1000”). Note that in the GL series the impeller
 248 rotation speed is fixed at $\Omega = 1500$ rpm since pronounced sedimentation was observed in the
 249 experiment at lower impeller rotation speeds. Finally, a special case “PE-dpS-vofL” is included
 250 since the corresponding experiment shows a particularly strong turbulence modulation.

251 The simulations are performed using ANSYS CFX release 21.1. A detailed discussion of the
 252 discretization schemes, the boundary conditions, and the implementation of the multiple-reference-
 253 frame approach (MRF) to treat the rotating parts can be found in Shi and Rzehak (2018, 2020).
 254 Here a summary is provided in section B of the Supplementary Material. [To match the experiment,](#)

255 a special procedure (Deen et al. 2002; Shi and Rzehak 2018) is applied during post processing for
 256 the present simulations to obtain the mean and fluctuating velocities in the inner, rotating MRF
 257 block. In particular, the axial profile of the mean velocity of both phases at a given radial position
 258 r is obtained by averaging all the results over the cylindrical surface defined by r . Details of this
 259 procedure are also given in section B of the Supplementary Material.

260

261 Table 2: Summary of the investigated cases and the corresponding power numbers predicted by the simulations.

name	Ω (rpm)	ρ_S/ρ_L (-)	$\bar{\alpha}_{S,ave}$ (%)	d_p (mm)	N_p (-)
single-phase	1500	-	-	-	3.64
cases concerning PE particles					
PE-base	1500	1.1	0.050	0.165	3.68
PE-vofS	1500	1.1	0.025	0.165	3.71
PE-vofL	1500	1.1	0.100	0.165	3.64
PE-rpm1000	1000	1.1	0.050	0.165	3.63
PE-rpm650	650	1.1	0.050	0.165	3.69
PE-dpS	1500	1.1	0.050	0.067	3.76
PE-dpL	1500	1.1	0.050	0.450	3.72
PE-dpS-vofL	1500	1.1	0.100	0.067	3.83
cases concerning GL particles					
GL-base	1500	2.5	0.050	0.165	3.67
GL-vofS	1500	2.5	0.025	0.165	3.69
GL-vofL	1500	2.5	0.100	0.165	3.69
GL-dpS	1500	2.5	0.050	0.067	3.74
GL-dpL	1500	2.5	0.050	0.425	3.62

262
 263 The mesh independency of the numerical results is assessed for three fully structured meshes
 264 (called mesh 144, mesh 180, and mesh 240) with increasing resolution. The numerical results for
 265 the mean and fluctuation velocities as well as the solid distribution are compared with the
 266 corresponding experimental results for the case GL-base (see Table 2). Details of the meshes and
 267 the comparison are provided in Appendix B. It turns out that to reduce the numerical error the mesh
 268 with the highest resolution, i.e. mesh 240, should be applied in principle. However, taking into
 269 account the required CPU time as well (see section C of the Supplementary Material), the
 270 compromise is made to apply mesh 180 as the default for all further simulations to be presented in
 271 this work. Results from mesh 240 will be included in addition where notable deviations between
 272 the computational and the experimental results are seen, in order to better reveal their origin.

273 Before discussing the spatially resolved results from the simulations, first the magnitude of the
 274 predicted power number, $N_{p,\Gamma} = 2\pi\Omega\Gamma/\rho_L\Omega^3D_i^5$ (with Γ denoting the torque acting on the impeller
 275 and the shaft) is checked, which is one of the most important and representative global
 276 dimensionless parameters for a stirred vessel. The numerical results obtained for each of the
 277 investigated cases are summarized in the last column of Table 2. In most of the investigated cases
 278 a power number around 3.6 is obtained which is significantly lower than the value of 5 from

279 Rushton et al. (1950), but in good agreement with the correlation of Bujalski et al. (1986). As
280 already discussed in the experimental work (Sommer et al. 2021), this is most likely due to the
281 relatively larger thickness of the impeller blades. A similar trend was observed in the experiments
282 of Rutherford et al. (1996) and Chapple et al. (2002) and the DNS simulation of Gillissen and Van
283 den Akker (2012).

284 An alternative approach to estimate the power number is to equate the power input to the total
285 energy dissipation rate. The power number obtained from this approach ($N_{p,\varepsilon}$) is always smaller than
286 that estimated from the torque ($N_{p,\Gamma}$). Moreover, with increasing grid resolution $N_{p,\Gamma}$ experiences
287 only a small variation, while $N_{p,\varepsilon}$ shows a gradual increase and reaches about 80 percent of $N_{p,\Gamma}$
288 based on the most refined mesh (mesh240) which comprises 13.8 million cells. A similar trend was
289 also reported in Coroneo et al. (2011) using the RANS approach. Moreover, in the DNS study by
290 Gillissen and Van den Akker (2012) $N_{p,\varepsilon}$ is still slightly smaller than $N_{p,\Gamma}$ even using 2.9 billion
291 grid cells. Based on these findings one may tentatively conclude that the underestimated power
292 number from the dissipation is mostly related to the inevitable truncation error, which is more
293 pronounced when a coarser grid is used.

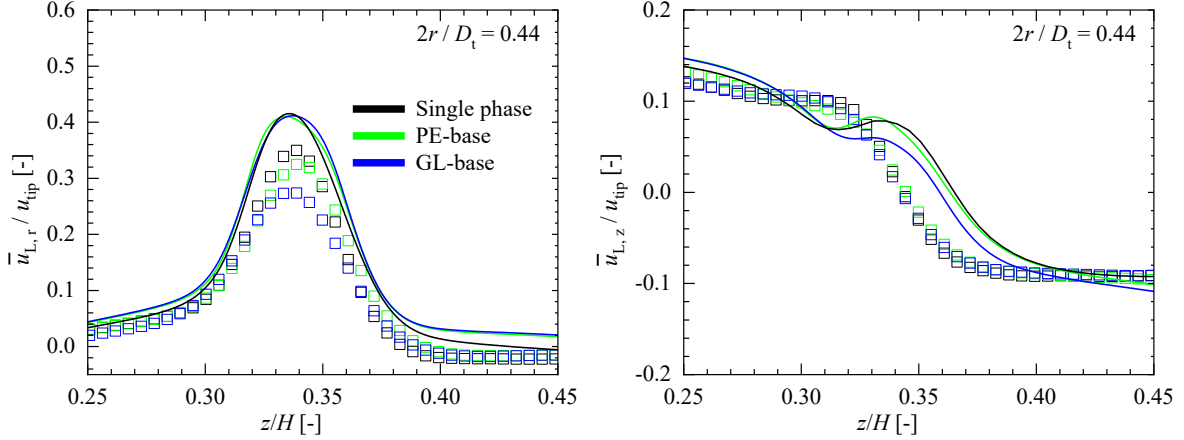
294 The remainder of this section discusses the simulation results for all cases listed in Table 2. More
295 specifically, section 3.1 provides a comprehensive discussion on the two “base” cases with
296 different types of particles. Section 3.2 outlines the effects of the operational parameters, i.e. the
297 particle size, the mean solid fraction, and the impeller rotation speed. No PIT model has been used
298 in obtaining the simulation results up to this point. To supplement this, section 3.3 presents results
299 obtained by different PIT models with a focus on the three typical cases: PE-base, GL-base, and
300 PE-dpS-vofL.

301 **3.1 Results for base cases**

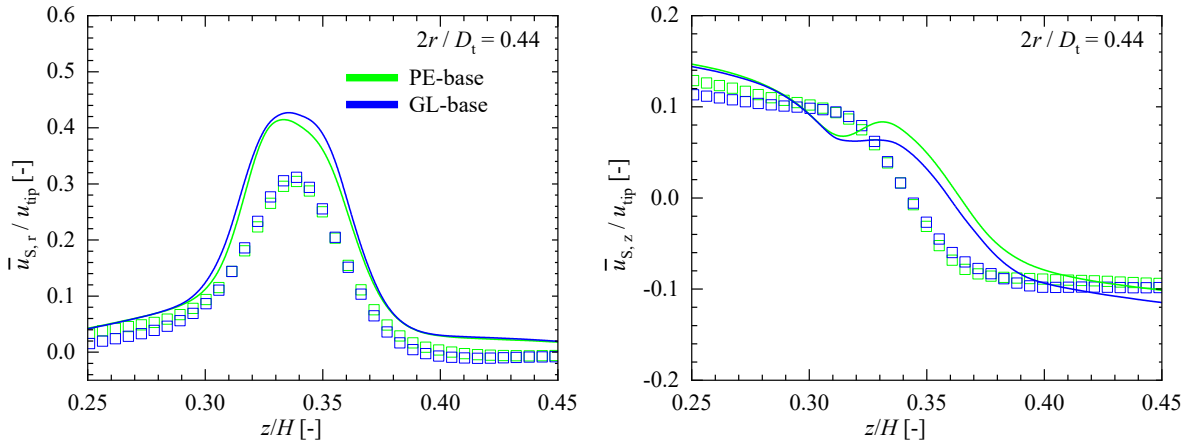
302 Results for the two base cases are discussed first to get an idea on the particle effects. Here, base
303 case corresponds to the situation with an impeller rotation speed of $\Omega = 1500$ rpm, a mean solid
304 fraction of $\bar{\alpha}_{s,ave} = 0.05\%$, and a mean particle diameter of $d_p = 0.165$ mm. PE-base
305 corresponds to the base case using PE particles which have a density ratio with respect to the liquid
306 phase of 1.1. Similarly, GL-base corresponds to the case with GL particles with a density ratio of
307 2.5. Results for the mean velocities, the solid fraction, and the fluctuating velocity of the liquid
308 phase are discussed in the following.

309 **3.1.1 Mean liquid and solid velocities**

310 Figure 1 summarizes the results for the mean liquid velocity obtained at a radial position $2r/D_t =$
311 0.44 near the tip of the impeller. With the presence of the particles, the experimental data reveal
312 no substantial change in the axial component of liquid velocity, but a notable decrease in the radial
313 component. In particular, in the case with GL particles the peak radial velocity is seen to decrease
314 by about 23% with a solid loading of only 0.05%. A further check on the data of Sommer et al.
315 (2021) indicates that a decrease by 14% already took place even with only 0.025% GL particles.
316 This decrease has also been observed in the recent experiment of Li et al. (2018) (their Fig. 15),
317 but for solid loadings of more than 1%. Compared with the experiment, simulation results show
318 relatively small particle effects on the liquid mean velocities. The agreement is ok far enough below
319 and above the impeller but not around it for both velocity components. This mismatch will be
320 picked up later together with the mean solid velocity.



321
 322 Figure 1. Axial profiles of the radial (left) and axial (right) components of the mean liquid velocity (normalized by the
 323 tip velocity of the impeller $u_{tip} = \pi D_t \Omega / 180$) at a radial position $2r/D_t = 0.44$. Solid lines: simulation results
 324 according to the model outlined in Table 1; symbols: experimental data from Sommer et al. (2021).

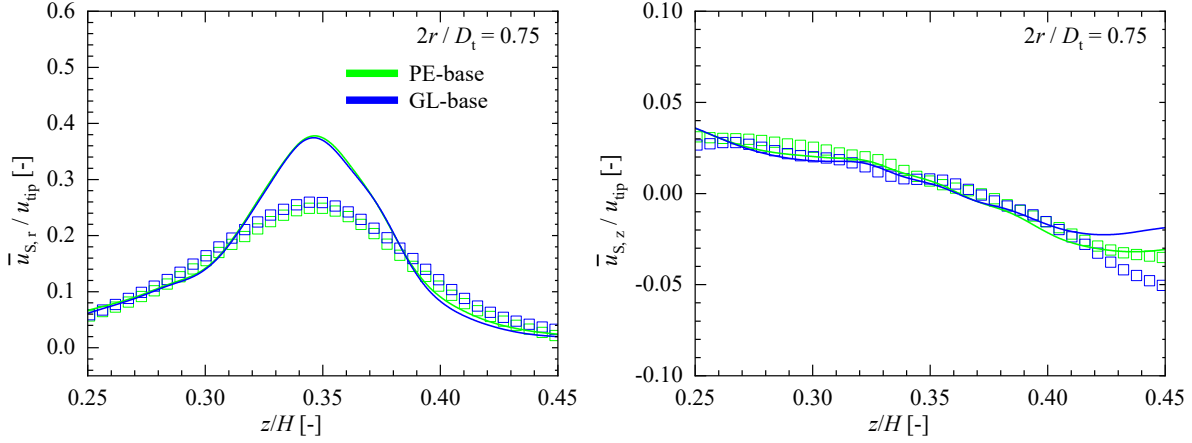


325
 326 Figure 2. As Figure 1 but for the solid phase: Polyethylene spheres (PE) and glass beads (GL).

327 Results for the mean solid velocities at the same radial position are shown in Figure 2. Both the
 328 experimental and the computational results show only a very small change in the solid velocities
 329 with increasing solid density (i.e. from PE-base to GL-base). This vanishingly small difference in
 330 the mean solid velocity indicates that for both particle types the inertia are still small. One may
 331 therefore expect their motion to mostly follow the mean liquid flow. This can be examined by
 332 checking the difference between the results shown in Figure 2 and Figure 1. It turns out that the
 333 above expectation applies for all simulation results and for the experimental data concerning PE
 334 particles, as the slip velocities revealed from these results are found vanishingly small. The
 335 experimental data concerning GL particles, however, indicate that the peak radial solid velocity is
 336 about 15% larger than that of the liquid phase. The present simulation is unable to reproduce this
 337 sizable slip.

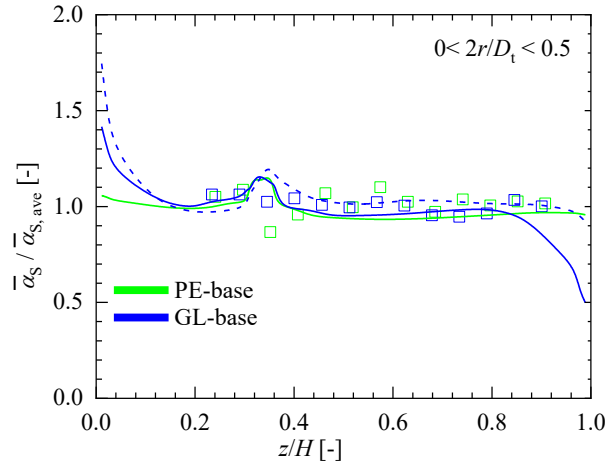
338 Figure 3 shows the results for the mean solid velocity at a radial position $2r/D_t = 0.75$. Similar to
 339 those in Figure 2, the difference between the experimental results obtained for PE and GL particles
 340 is negligibly small. Owing to the spreading of the impeller stream, the mean velocity of both phases
 341 decreases with increasing radial distance. Compared with Figure 2, experimental results indicate a
 342 decrease in the peak of the radial velocity of about 0.05 (normalized by u_{tip}) for both types of

343 particles. This decrease is qualitatively captured by the simulations, although the magnitude of the
 344 peak values is overestimated at these two radial positions. In comparison, the decrease in the axial
 345 component of the mean velocity is more pronounced. At $2r/D_t = 0.44$ the magnitude of the
 346 maximum axial velocity in the considered axial range is around 0.1, while it has decreased by a
 347 factor of 2 at $2r/D_t = 0.75$. Simulation results reproduce these changes and show quite good
 348 agreement with the experimental data.



349
 350 Figure 3. As Figure 1 but for the solid velocity at a radial position $2r/D_t = 0.75$ far away from the impeller.

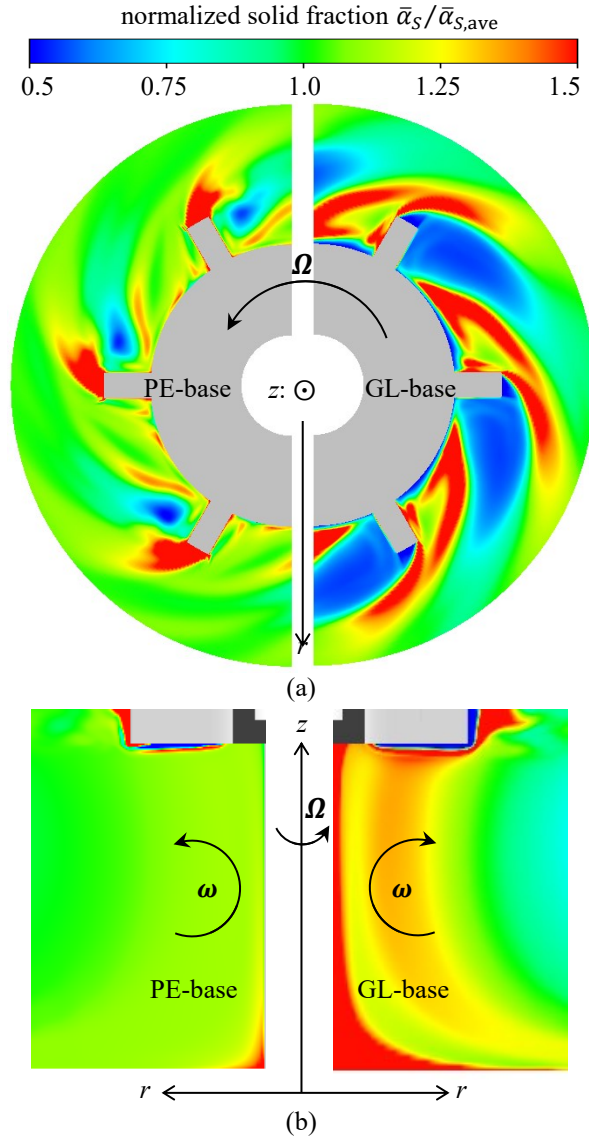
351 3.1.2 Solid fraction



352
 353 Figure 4. Results for the horizontally averaged solid fraction along the height of the tank. Solid (dashed) lines:
 354 present simulation results from mesh 180 (mesh 240); symbols: experimental data from Sommer et al. (2021).

355 Results for the solid fraction along the height of the tank are shown in Figure 4. At each z/H , $\bar{\alpha}_s$
 356 corresponds to the area-averaged solid fraction in the horizontal plane defined by z/H for $0 <$
 357 $2r/D_t \leq 0.5$. For both cases, experimental data available for $0.2 < z/H < 0.9$ show no significant
 358 variation along the height, indicating the suspension being rather homogenous. Only in the region
 359 near the impeller (i.e. at $z/H \approx 0.33$), the solid fraction for PE particles is about 15% lower than
 360 the mean value. Simulation results show generally good agreement with the experimental data with
 361 two exceptions. One is the region near the tank top where the calculated solid fraction for GL
 362 particles decreases with increasing z/H , in contradiction to the experiment. This mismatch is a

363 numerical error caused by the applied mesh (mesh 180, see section B of the Supplementary
 364 Material for details), which was chosen for reasons of CPU time despite its somewhat too low
 365 resolution, and can be eliminated using the more refined mesh, i.e. mesh 240 (see the dashed line
 366 in Figure 4). Interestingly, the result for the PE-base case, which is obtained also using mesh 180,
 367 agrees well with the measured data in this region. Not surprisingly this indicates a possible
 368 dependency of the required mesh resolution on the particle properties (here, density).



369
 370 Figure 5. Simulation results for the solid fraction (normalized by $\bar{\alpha}_{s,ave}$) in (a) the horizontal plane $z/H = 0.33$ (i.e.
 371 at the center of the impeller) for $0 < 2r/D_t \leq 0.5$ and (b) the vertical plane located midway between two baffles for
 372 $0 < 2r/D_t \leq 0.5$ and $0 < z/H \leq 0.4$. In both (a) and (b) the left and right panels correspond to the cases PE-base and
 373 GL-base, respectively. The impeller rotation Ω is along the z axis, i.e. in the anticlockwise direction in (a).

374 The other and more interesting exception where the simulations results deviate from the
 375 experimental data occurs in the region near the impeller. As shown in Figure 4, there the predicted
 376 solid fractions are larger than both the mean value $\bar{\alpha}_{s,ave}$ and the experimental results. To better

377 understand this deviation, the predicted solid fraction in the horizontal plane at the center of the
378 impeller is examined. The results for both particles are shown in Figure 5 (a). It turns out that a
379 large amount of particles accumulates in the vicinity of the impeller tips. Meanwhile, a region with
380 lower-than-average solid fraction exists behind the impeller blades (note that in Figure 5 (a) the
381 impeller rotates along the z axis, i.e. in the anticlockwise direction), which is more pronounced for
382 GL particles. Such a highly non-uniform distribution of particles at the center of the impeller has
383 also been reported in Derksen (2003, Fig. 3), where a highly resolved simulation based on the E-L
384 / LES approach has been conducted. Averaging the values over the horizontal plane gives a higher-
385 than-average solid fraction for both particles, i.e. the higher-concentration region outweighs the
386 lower one.

387 In Figure 4, the calculated solid fractions for GL and PE particles deviate from each other when
388 approaching the tank bottom (i.e. with z/H decreasing from 0.2 to 0). More specifically, for GL
389 particles the profile sharply increases towards a distinct maximum at the tank bottom, while for PE
390 particles it shows only a small variation reaching a maximum that is only slightly larger than the
391 mean value. These different behaviors may be better understood by checking the solid fraction
392 distribution in the vertical plane midway between two baffles underneath the impeller for $0 <$
393 $2r/D_t \leq 0.5$ as shown in Figure 5 (b). These results indicate that in the lower part of the tank PE
394 particles are still rather homogeneously suspended, while GL particles accumulate in the tank center
395 especially when approaching the tank bottom.

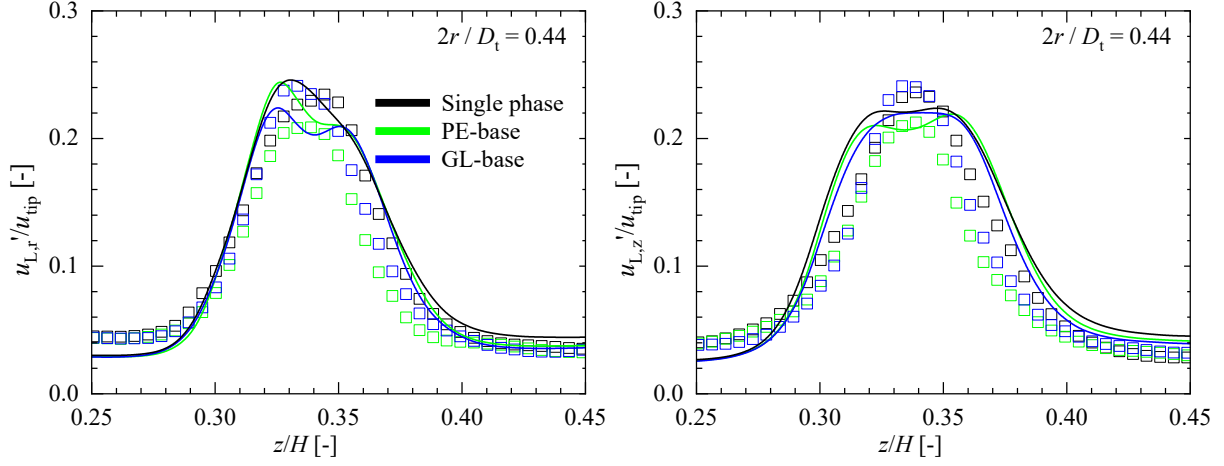
396 The latter behavior has also been observed in the highly resolved simulation of Derksen (2003, Fig.
397 3). The underlying mechanism is outlined in the following. First, it is noted that, when the impeller
398 is initially at rest, both particles would deposit at the bottom, owing to their larger density compared
399 with that of the ambient liquid. Impeller rotation generates two counter rotating vortices in the
400 vertical plane underneath the impeller. Their orientations as characterized by the flow vorticity ω
401 are illustrated in Figure 5 (b). The associated mean flow carries the accumulated particles at the
402 bottom first to the tank center and then upwards to the impeller. Particle suspension driven by this
403 advection mechanism is certainly more efficient for particles with less inertia, making the
404 distribution of PE particles more homogenous than that of GL particles. Nevertheless, as seen in
405 Figure 5 (b), a high solid fraction is present at the bottom closest to the tank center even for PE
406 particles, owing to the relatively weak mean-flow advection in this region.

407 3.1.3 Fluctuation of liquid velocity

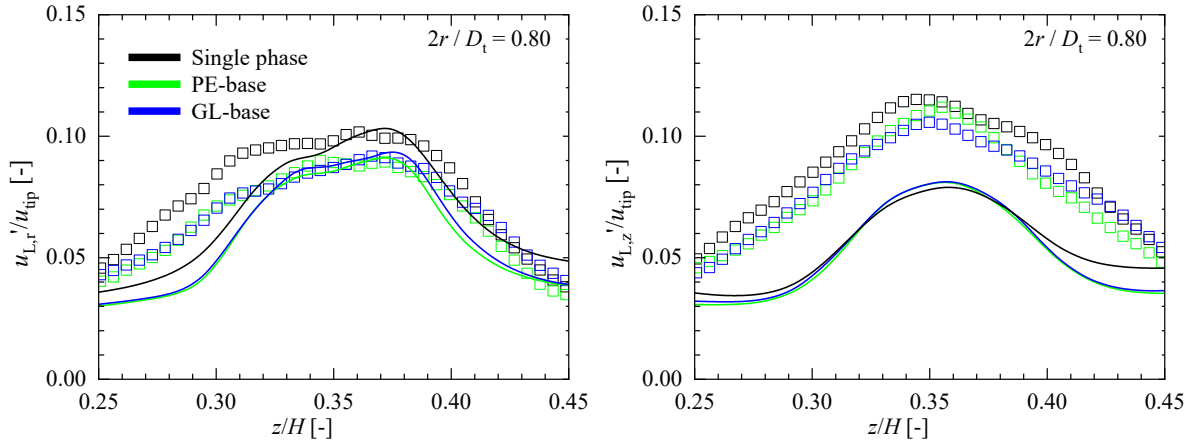
408 Figure 6 and Figure 7 summarize the results for the liquid velocity fluctuation at two radial
409 positions of $2r/D_t = 0.44$ and 0.80 , respectively. Experimental results indicate that near the
410 impeller at $2r/D_t = 0.44$, the peak of both the radial ($u'_{L,r}$) and axial ($u'_{L,z}$) components of
411 fluctuation in the PE-base case are about 10% smaller than their counterparts in the single-phase
412 case. In comparison, the change caused by GL particles is seen to be relatively small. Farther away
413 from the impeller at $2r/D_t = 0.80$, the reduction in the peak caused by PE particles almost
414 vanishes and hardly any difference between the data for the two particle-laden cases can be
415 observed.

416 Turning to the simulation results, good agreement with the experimental data is achieved in the
417 single-phase case at $2r/D_t = 0.44$, while at $2r/D_t = 0.80$ in particular the axial fluctuation is
418 underestimated by about 30%. Compared to the single-phase case, the presence of both particles
419 tends to suppress the liquid velocity fluctuation at both radial positions in the simulations. This is
420 in qualitative agreement with the experimental observation with the only exception being the radial

421 fluctuation profiles in the GL-base case at $2r/D_t = 0.44$. There, compared with the single-phase
 422 results, the peak value is seen to decrease in the simulation, instead of remaining unchanged as
 423 reported in the experiment.



424
 425 Figure 6. Axial profiles of the radial (left) and axial (right) components of the liquid velocity fluctuation at a radial
 426 position $2r/D_t = 0.44$ close to the impeller. Lines: present simulation results; symbols: experimental data from
 427 Sommer et al. (2021).

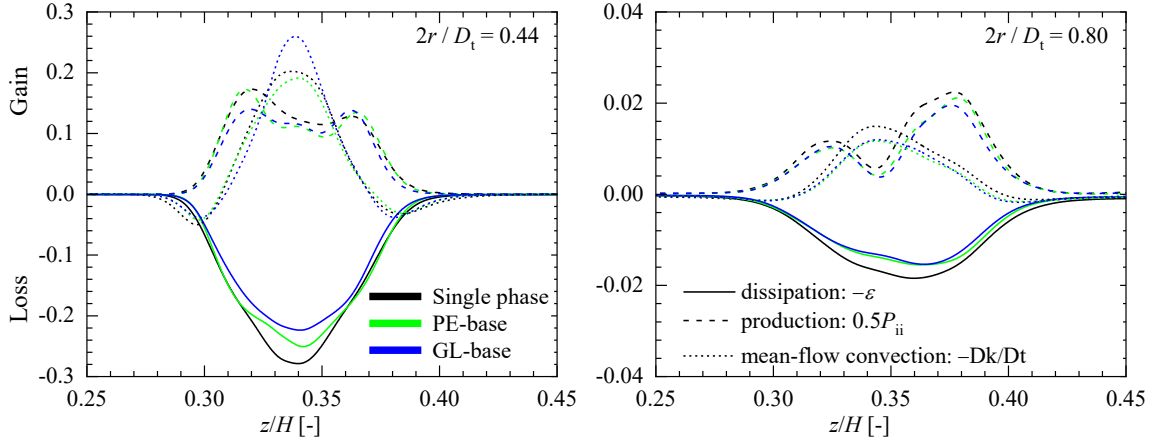


428
 429 Figure 7. As Figure 6 but at a radial position $2r/D_t = 0.80$ far away from the impeller.

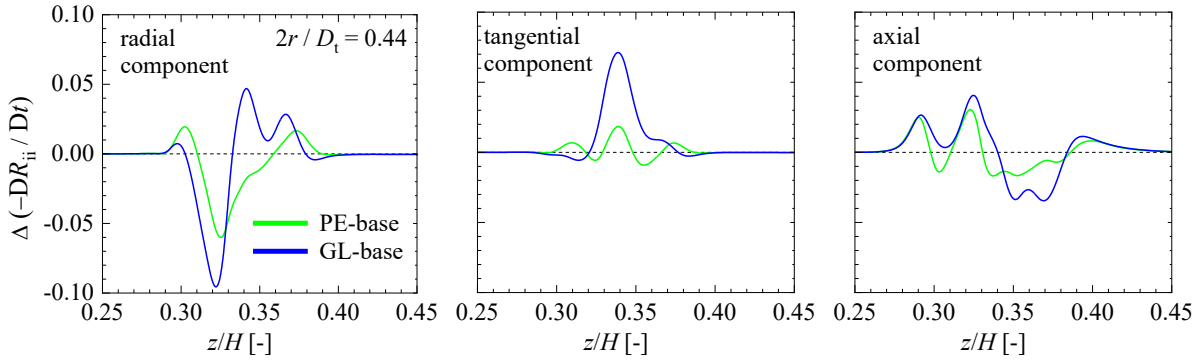
430 Since no PIT model is applied in the two-phase simulations the notable variation with respect to
 431 the single-phase results is unexpected at first glance. To seek the origin of this variation, the budget
 432 of the turbulent kinetic energy $k = R_{ii}/2$ is shown in Figure 8 at two radial positions of $2r/D_t =$
 433 0.44 and 0.80 . For the sake of brevity, results are shown only for the production ($P_{ii}/2$), the
 434 dissipation ($-\varepsilon$), and the mean-flow convection ($-Dk/Dt$). The variation in the diffusion ($\nabla \cdot$
 435 $[\alpha(\mu^{\text{mol}} + C_s \mu^{\text{turb}}) \nabla k]$) can be estimated based on the balance of the budget equation. As seen
 436 from the different scales of the two panels, the contributions at $2r/D_t = 0.44$ are at least an order
 437 of magnitude larger than their counterparts at $2r/D_t = 0.80$.

438 In the single-phase case, the dissipation and the convection at $2r/D_t = 0.44$ reach their maximum
 439 at approximately $z/H = 0.34$, a position at which the mean radial flow reaches its maximum as
 440 well (left panel of Figure 1). Away from the peak, their magnitudes gradually decrease and are

441 nearly symmetric with respect to the position $z/H = 0.34$, a feature that has also been observed in
 442 jet flows (Pope 2000, chapter 5). At the same radial position, the production shows a double-peaked
 443 profile, featuring a local minimum at $z/H = 0.34$ and two local maxima about $0.02H$ away on
 444 each side. Unlike the dissipation and convection, the production is asymmetrically distributed with
 445 the lower (upper) part contributing more (less) energetically to the turbulent kinetic energy at
 446 $2r/D_t = 0.44$ (0.80).



447
 448 Figure 8. Simulation results for the budget of the turbulent kinetic energy [based on Eq. (3)] at two radial positions of
 449 $2r/D_t = 0.44$ (left) and $2r/D_t = 0.80$ (right). Results are shown for the three major contributions, i.e. the dissipation,
 450 the production, and the mean-flow convection (denoted by different type of lines). All quantities are normalized by
 451 u_{tip}^3/D_t .



452
 453 Figure 9. Change in the mean-flow convection of the normal Reynolds stresses caused by the particles.

454 In the two-phase cases, the shapes of the profiles remain the same, but the predicted dissipation is
 455 seen to be smaller than in the single phase case, in agreement with previous experimental
 456 observations in particle-laden stirred-tank flows (Unadkat et al. 2009, Gabriele et al. 2011, Chen
 457 et al. 2011). The production term also experiences a reduction by both particles, which roughly
 458 balances the decrease in dissipation in the case with PE particles. The predicted turbulence
 459 modulation can be mostly understood by checking the variation in the convection, which is seen to
 460 depend on the position. At $2r/D_t = 0.44$ (left panel of Figure 8), a slight reduction is seen in the
 461 PE-base case, making the predicted fluctuation decrease. Meanwhile, a significant increase in the
 462 peak of the convection is seen in the GL-base case.

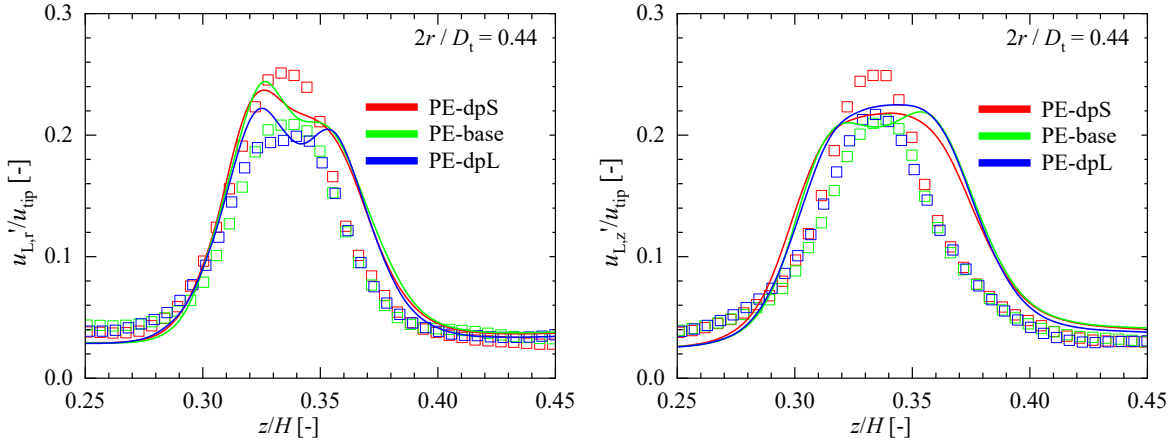
463 Closer inspection indicates that the redistribution of this increase is anisotropic. This is revealed in
 464 Figure 9, where the difference in the convection of the three normal Reynolds stresses to the single-

465 phase results, i.e. $\Delta \left(-\frac{DR_{ii}}{Dt} \right)$, is illustrated. It is seen that only the tangential component in the GL-
 466 base case (blue line in the middle panel of Figure 9) experiences a significant increase. Meanwhile,
 467 compared with the results in the PE-base case, the radial component exhibits a larger decrease in
 468 the region near the impeller tip (i.e. for $z/H = 0.33$). This latter behavior leads to a larger reduction
 469 in the radial fluctuation as seen in Figure 6. At $2r/D_t = 0.80$ (Figure 8), all three terms are
 470 suppressed by particles, but the combined reduction in the production and the convection surpasses
 471 that in the dissipation, causing both components of the fluctuation to decrease as seen in Figure 7.

472 3.2 Effects of operational parameters

473 This section discusses the effects of the operational parameters on the two-phase flow field. These
 474 comprise effects of the particle size, the mean solid fraction, and the impeller rotation speed. It
 475 turns out both in the simulations and in the experiment that only the liquid velocity fluctuation and
 476 the solid fraction are significantly affected by these parameters. These will therefore be the focus
 477 of the discussion in the following.

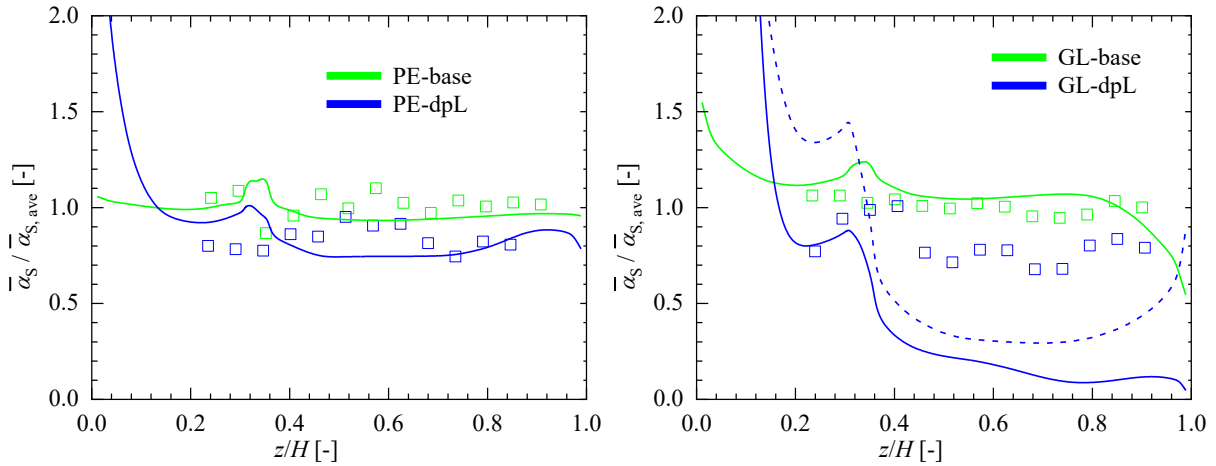
478 3.2.1 Particle size



479 Figure 10. Axial profiles of the radial (left) and axial (right) components of liquid velocity fluctuation at a radial
 480 position $2r/D_t = 0.44$ in cases with different sizes of PE particles. Lines: simulation results; symbols: experimental
 481 data from Sommer et al. (2021). Case details: $\Omega = 1500$ rpm, $\rho_S/\rho_L = 1.1$, and $\bar{\alpha}_{S,ave} = 0.05\%$ in all cases; the particle
 482 diameters are 0.067 mm, 0.165 mm, and 0.425 mm in the dpS, base, and dpL cases, respectively.
 483

484 For both the PE and the GL particles, three different sizes with $d_p = 0.067, 0.165$, and
 485 ~ 0.425 mm are considered. The corresponding results are denoted as “dpS”, “base”, and “dpL”,
 486 respectively. Concerning the liquid velocity fluctuation, it is revealed both by the computations
 487 and by the experiment that more pronounced size effects occur for the PE than for the GL particles.
 488 Therefore, only the results involving PE particles will be discussed. Figure 10 summarizes the
 489 results for the radial and the axial components of the fluctuation at $2r/D_t = 0.44$. Experimental
 490 results indicate a tendency of increasing peak for both the radial and axial fluctuations with
 491 decreasing particle size. Simulation results for the radial fluctuation qualitatively reproduce this
 492 tendency. For the predicted profiles of the axial fluctuation, however, no notable trend could be
 493 observed. This mismatch is likely due to the lack of PIT model in the present simulations and will
 494 be examined in more detail in section 3.3.

495 Figure 11 summarizes the results for the horizontally averaged solid fraction for PE (left panel)
 496 and GL (right panel) particles. Since experimental results were not provided for the smallest size
 497 (i.e. dpS), results are shown only for the two larger ones. With the particle size increasing from
 498 base to dpL, experimental results available in the axial portion away from the tank bottom (i.e. for
 499 $z/H > 0.2$) reveal a reduction in the averaged solid fraction, which is more pronounced for GL
 500 particles. Mass conservation yields that the solid fraction in the residual portion, i.e. the region
 501 close to the tank bottom, must be much higher than the mean value. This variation is confirmed by
 502 the simulations. In particular, for both particles, the predicted solid fraction for $z/H < 0.1$ in the
 503 two dpL cases is significantly larger than that in the two base cases. Compared with the
 504 experimental results, good agreement is achieved for PE particles of both sizes; for the larger GL
 505 particles, however, a significant underestimation takes place for $z/H > 0.3$.



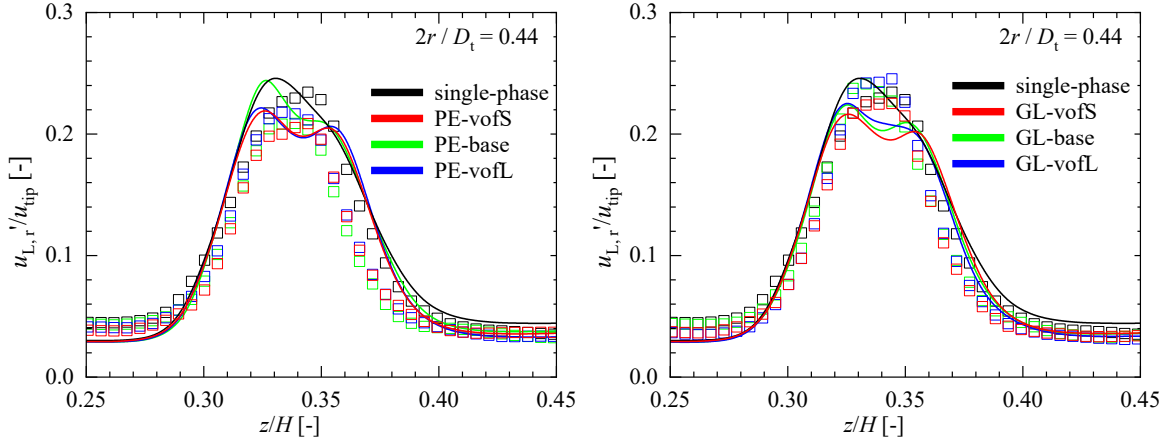
506
 507 Figure 11. Results for the horizontally averaged volume fraction of PE (left, i.e. $\rho_S/\rho_L = 1.1$) and GL (right, i.e. ρ_S/ρ_L
 508 $= 2.5$) particles along the height of the tank in cases with different particle sizes. Solid (dashed) lines: simulation results
 509 from mesh 180 (240); symbols: experimental data from Sommer et al. (2021). Case details: $\Omega = 1500$ rpm and $\bar{\alpha}_{S,ave} = 0.05\%$
 510 $= 0.05\%$ in all cases; the particle diameters are 0.165 mm and 0.425 mm in the base and dpL cases, respectively.

511 The deviation in the GL-dpL case might be due to the applied mesh, the resolution of which was
 512 found too low to reproduce the experimental results for the GL-base case near the top of the tank.
 513 To check this possibility, an additional run for the GL-dpL case based on mesh 240 (see section B
 514 of the Supplementary Material for details) is conducted. The corresponding prediction appears in
 515 the right panel of Figure 11 as a dashed line. Comparing the two blue lines reveals a moderate
 516 increase in the solid fraction in the region above the impeller with increasing mesh resolution.
 517 Moreover, the difference in the results from the two meshes is more pronounced than that revealed
 518 in the GL-base case (see Figure 4), indicating that the resolution of mesh 240 might be still
 519 insufficient for the GL-dpL case. Assessment of meshes beyond mesh 240, however, is
 520 unaffordable based on the available computational resources.

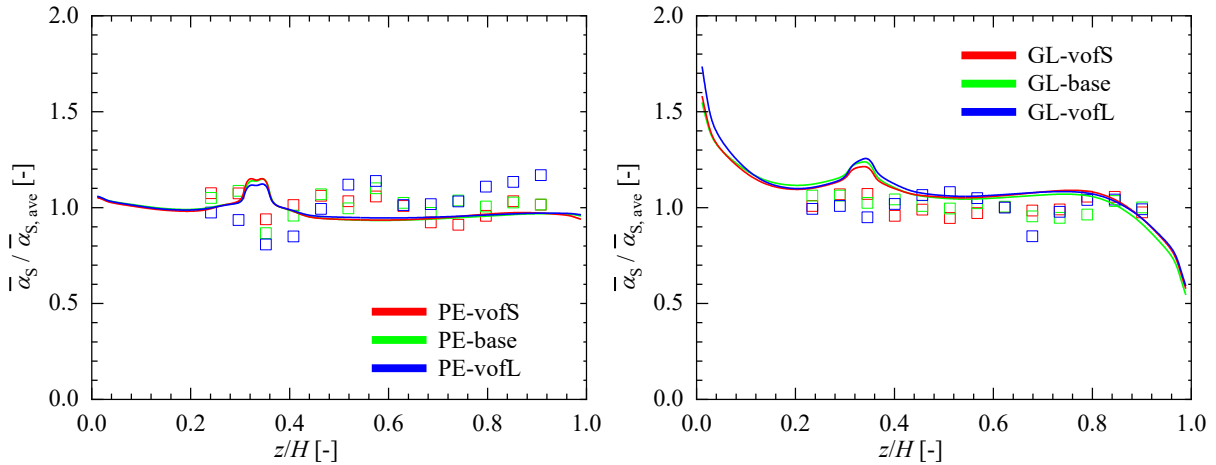
521 3.2.2 Mean solid fraction

522 Three different mean solid fractions with $\bar{\alpha}_{S,ave} = 0.025\%$, 0.05% , and 0.1% are considered for
 523 both the PE and the GL particles. The corresponding results are denoted by “vof”, “base”, and
 524 “vofL”, respectively.

525 Figure 12 shows some of the typical results for the liquid velocity fluctuation obtained at a radial
 526 position $2r/D_t = 0.44$. Only results for the radial fluctuation are presented as those for the axial
 527 ones show similar features. In view of the experiment, it is seen that the presence of PE particles
 528 (left panel) tends to decrease the liquid fluctuation in particular when the solids loading is low. As
 529 for the GL results (right panel), a moderate increase in the liquid fluctuation with increasing mean
 530 solid fraction can be observed. These observations are well reproduced by the simulations.



531
 532 Figure 12. Axial profiles of the radial fluctuation at a radial position $2r/D_t = 0.44$ in cases with different loading of
 533 PE (left, i.e. $\rho_S/\rho_L = 1.1$) and GL (right, i.e. $\rho_S/\rho_L = 2.5$) particles. Lines: simulation results; symbols: experimental
 534 data from Sommer et al. (2021). Case details: $\Omega = 1500$ rpm and $d_p = 0.165$ mm in all cases; the mean solid volume
 535 fractions are 0.025%, 0.05%, and 0.1% in the vofS, base, and vofL cases, respectively.

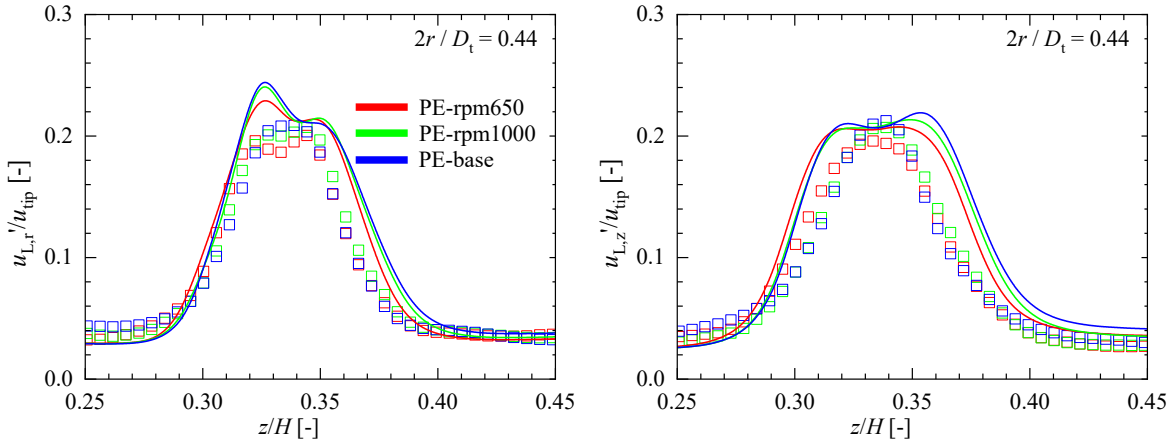


536
 537 Figure 13. Results for the horizontally averaged volume fraction of PE (left) and GL (right) particles along the height
 538 of the tank in cases with different loading of particles. Lines, symbols, and case details as in Figure 12.

539 Figure 13 summarizes the results for the horizontally averaged solid fraction along the height of
 540 the tank. Experimental results show no definite trend in the normalized value with increasing mean
 541 solid fraction; the relatively scattered results in the two cases with highest solid loading are likely
 542 a consequence of the experimental uncertainty. Simulation results also show a vanishingly small
 543 effect of the mean solid fraction and achieve quite good quantitative agreement with the
 544 experimental results.

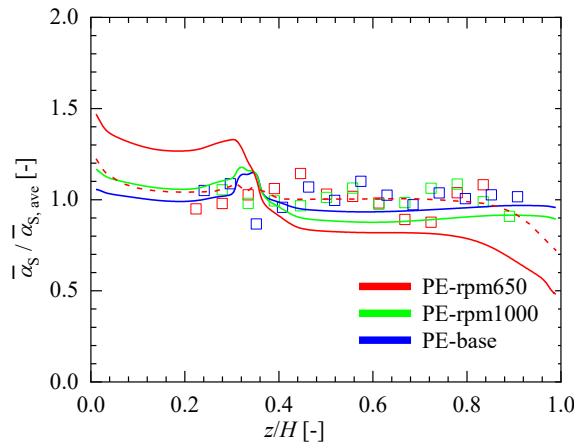
545 3.2.3 Impeller rotation speed

546 Three different impeller rotation speeds of $\Omega = 650, 1000,$ and 1500 rpm are considered. Only
 547 cases with PE particles are simulated, as in the corresponding cases with GL particles no complete
 548 suspension could be achieved at the lower two impeller rotation speeds in the experiment. The
 549 results obtained at these three different impeller rotation speeds are denoted by “rpm650”,
 550 “rpm1000”, and “base”, respectively.



551
 552 Figure 14. Axial profiles of the radial (left) and axial (right) components of the liquid velocity fluctuation in the three
 553 PE-laden cases, i.e. $\rho_S/\rho_L = 1.1$, with different impeller rotation speeds at a radial position $2r/D_t = 0.44$. Lines:
 554 simulation results; symbols: experimental data from Sommer et al. (2021). Case details: $d_p = 0.165$ mm and $\bar{\alpha}_{S,ave} =$
 555 0.05% in all cases; the impeller rotation speeds are 650 rpm, 1000 rpm, and 1500 rpm in the rpm650, rpm1000, and
 556 base cases, respectively.

557 Results for the liquid velocity fluctuation at a radial position $2r/D_t = 0.44$ are summarized in
 558 Figure 14. Experimental results indicate that, when normalized by the corresponding impeller tip
 559 velocity, the peaks of both the radial (left panel) and the axial (right panel) components of velocity
 560 fluctuation show a tiny decrease with decreasing impeller rotation speed, which is qualitatively
 561 reproduced by the simulations.

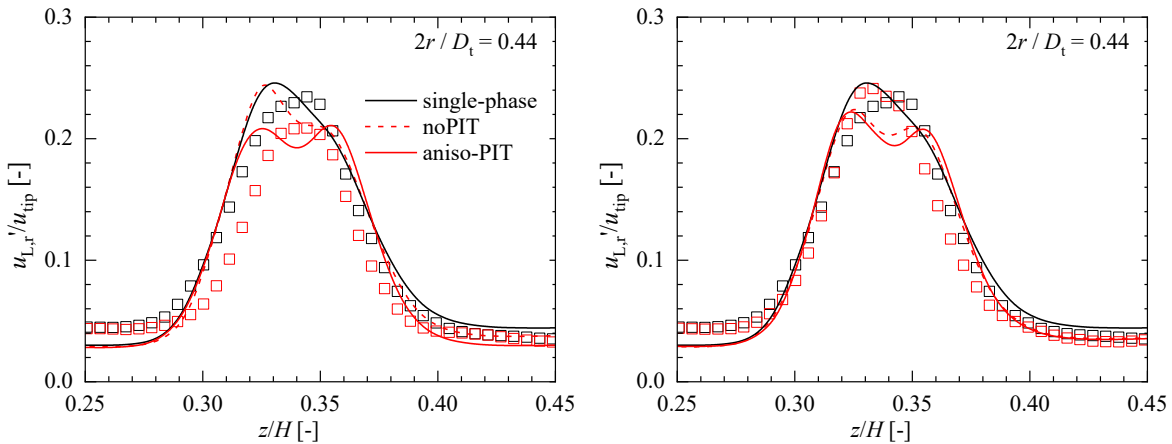


562
 563 Figure 15. Results for the horizontally averaged volume fraction of PE particles along the height of the tank in cases
 564 with different impeller rotation speeds. Lines, symols, and case details as Figure 14.

565 Figure 15 compares the results for the horizontally averaged solid fraction obtained at the three
 566 different impeller rotation speeds. The experiment shows no definite trend in the results obtained
 567 at all three impeller rotation speeds, indicating that the flow is already in the fully suspended state
 568 at the lowest impeller rotation speed (i.e. at $\Omega = 650$ rpm). Similarly, simulation results obtained
 569 at the larger two impeller rotation speeds show only slight deviation; their agreement with the
 570 corresponding experimental results is also as expected. At the lowest impeller rotation speed,
 571 however, simulation results differ from the experiment. In particular, the predicted solid fraction
 572 in the region beneath the impeller is approximately 30% higher than the mean value, leading to a
 573 moderate underestimation of the experimental results in the region above the impeller. This
 574 mismatch may be a consequence of insufficient mesh resolution, which has been shown to cause
 575 similar deviation for GL particles (Figure 11). This is confirmed by the results of an additional run
 576 using mesh 240 (dashed line in the right panel of Figure 15), according to which the flow at $\Omega =$
 577 650 rpm is in the fully suspended state, in agreement with the corresponding experimental results.

578 **3.3 Performance of available PIT models**

579 Experimental results shown in the last two sections revealed notable turbulence modulation by the
 580 particles. Although no PIT model has been employed, the simulation results are capable to
 581 qualitatively reproduce the particle effects. To improve quantitative predictions, however, the PIT
 582 should be taken into account as well. This is feasible by combining the closure models outlined in
 583 section 2.1 with the PIT models summarized in section 2.2. Following this methodology, the
 584 performance of the various PIT models is assessed in this section. To reduce the computational
 585 effort, three typical cases are considered, namely PE-base, GL-base, and PE-dpS-vofL (see Table
 586 2 for the case details), in which the liquid fluctuations were observed in the experiment to be
 587 suppressed, unaffected, and augmented.

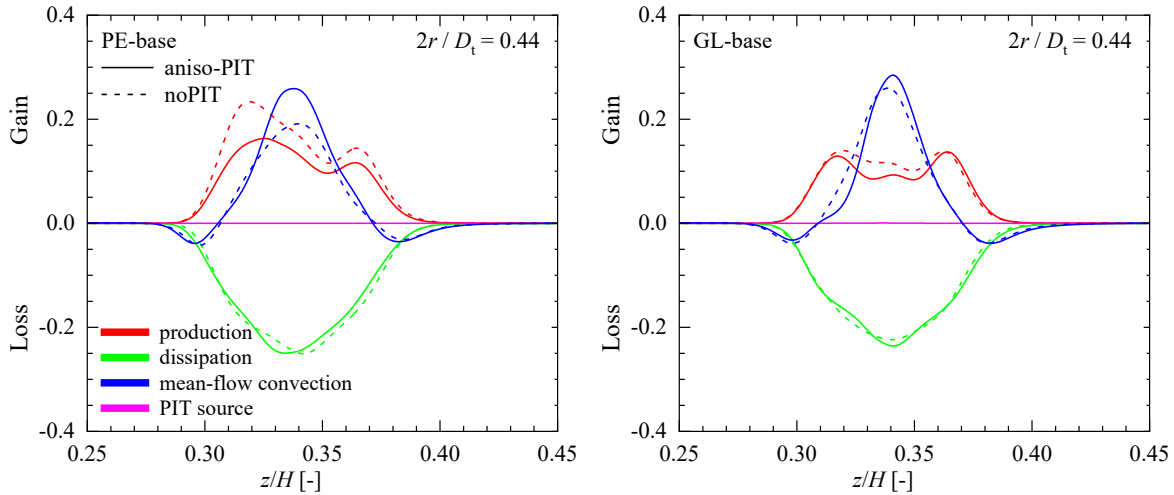


588
 589 Figure 16. Axial profile of the radial component of the liquid velocity fluctuation at a radial position $2r/D_t = 0.44$.
 590 Black symbols (line) denote the experimental (computational) results in the single-phase case. Red symbols (lines) in
 591 the left and right panels correspond to the experimental (computational) results in the PE-base and GL-base cases,
 592 respectively.

593 The aniso-PIT model is assessed first, as it represents the best currently available description. The
 594 predictions are compared with those obtained without adopting any PIT model (denoted as “noPIT”)
 595 to gain an idea on the performance of this model. Figure 16 provides some of the typical results for
 596 the radial component of the liquid velocity fluctuation obtained for the two base cases. In the case
 597 PE-base (left panel), the prediction without the PIT model shows only a slight turbulence

598 suppression (comparing the red dashed line with the black solid line), while moderate turbulence
 599 suppression is seen in the experiment. This mismatch is eliminated by adopting the anisotropic PIT
 600 model. In particular, the sizable reduction in the peak of the fluctuation is more satisfactorily
 601 reproduced. In the case with GL particles, both predictions show a moderate decrease in the peak,
 602 and virtually no difference between the two predictions can be observed; in the experiment,
 603 however, hardly any turbulence modulation by GL particles can be observed.

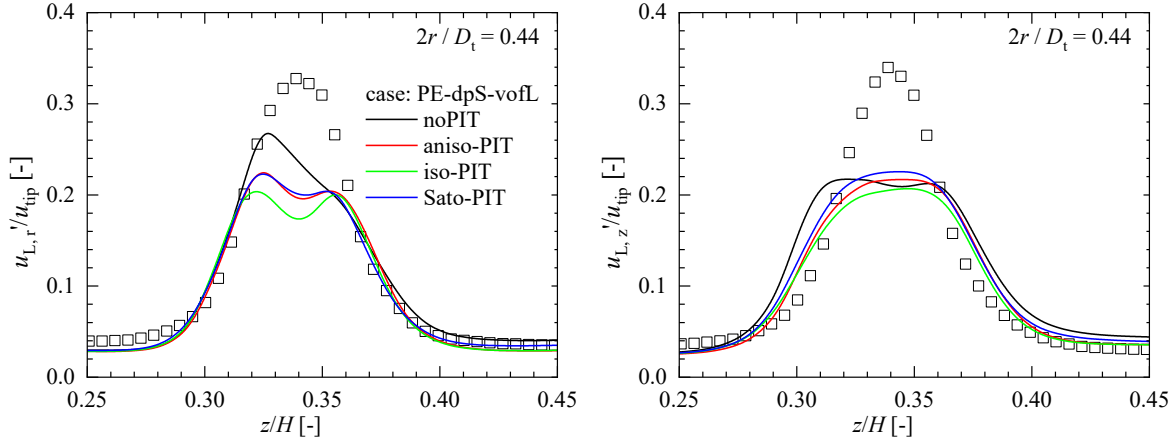
604 The weak turbulence modulation revealed in the GL-base case is a bit surprising, although this is
 605 also confirmed by the experiment. Since the inertia of GL particles is greater, the resulting
 606 turbulence modulation is expected to be stronger than that by PE particles. To further clarify why
 607 this is not observed, the difference between the budgets of the turbulent kinetic energy, based on
 608 Eq. (3), obtained with and without the addition of the anisotropic PIT model is examined. The
 609 production ($0.5P_{ii}$), dissipation ($-\varepsilon$), mean-flow convection ($-Dk/Dt$), and PIT-source ($S^k/\alpha_L\rho_L$)
 610 obtained in the two base cases are shown in Figure 17. For both cases, the source by PIT is
 611 vanishingly small compared with the other terms. In addition, it can be observed that virtually no
 612 change in the dissipation is caused by the anisotropic PIT model. In the production term in contrast,
 613 it causes a notable reduction, which is more pronounced for PE particles. This reduction is only
 614 partially compensated by the increase in the mean-flow convection, leading to a reduction in the
 615 liquid velocity fluctuation in particular in the PE-base case as seen in Figure 16.



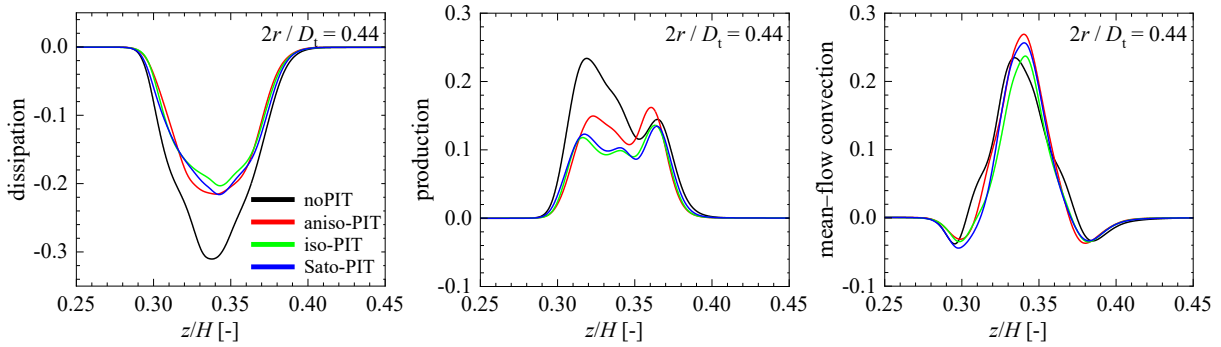
616
 617 Figure 17. Simulation results for the turbulent-kinetic-energy budget in the two cases of PE-base (left) and GL-base
 618 (right) at a radial position $2r/D_t = 0.44$. Different colors denote different terms as detailed in the left panel. All
 619 quantities are normalized by u_{tip}^3/D_t .

620 The assessment proceeds by considering the case PE-dpS-vofL, in which the liquid is loaded with
 621 PE particles with a diameter of ~ 0.067 mm and a volume fraction of 0.1%. All three different PIT
 622 models introduced in section 2.2, i.e. aniso-PIT, iso-PIT, and Sato-PIT, are tested. Figure 18
 623 compares the predictions for the liquid velocity fluctuation with the experimental results at
 624 $2r/D_t = 0.44$. The measured peaks of both the radial and axial components of the fluctuation are
 625 seen to be approximately 50% larger than their counterparts in the single-phase case (black symbols
 626 in Figure 16). This augmentation is not reproduced by any of the simulations. Rather, comparing
 627 the simulation results with those in the single-phase case (black lines in Figure 16) reveals a
 628 turbulence suppression by the particles. This suppression is seen to be more pronounced in the

629 radial component in simulations with PIT models, i.e. the prediction is deteriorated by all PIT
 630 models.



631
 632 Figure 18. Axial profiles of the radial (left) and axial (right) components of the liquid velocity fluctuation in the case
 633 PE-dpS-voFL at a radial position $2r/D_t = 0.44$. Lines: simulation results by different models distinguished by colors;
 634 symbols: experimental data from Sommer et al. (2021). Case details: $\Omega = 1500$ rpm, $\rho_S/\rho_L = 1.1$, $\bar{\alpha}_{S,ave} = 0.1\%$, $d_p \approx$
 635 0.067 mm.



636
 637 Figure 19. Simulation results for the turbulent-kinetic-energy budget in the case PE-dpS-voFL at a radial position
 638 $2r/D_t = 0.44$. Left: dissipation; middle: production; right: mean-flow convection. All quantities are normalized by
 639 u_{tip}^3/D_t .

640 To figure out the cause of this deterioration, again the budget of the turbulent kinetic energy is
 641 examined. Figure 19 presents the simulation results for the dissipation (left panel), the production
 642 (middle panel), and the mean-flow convection (right panel). Results for the PIT-source obtained in
 643 the two simulations applying the anisotropic (aniso-PIT) and the isotropic (iso-PIT) models,
 644 respectively, are not shown, as their magnitudes are again vanishingly small compared with the
 645 three terms above.

646 Concerning the dissipation, its magnitude is seen to be smaller in all simulations taking into account
 647 the PIT effects than that obtained in the simulation without PIT. This is encouraging as turbulence
 648 augmentation could be anticipated if all the other terms in the budget equation remained unchanged.
 649 However, as revealed in the middle and right panels of Figure 19, this is the case only for the mean-
 650 flow convection. For the production all models taking into account the PIT effects exhibit a
 651 significant reduction. Given that the PIT-source term is vanishingly small, this reduction causes a
 652 suppression of the calculated liquid fluctuation for all of these models. Close inspection of the two

653 results applying the anisotropic and the isotropic PIT models indicates a more pronounced
654 reduction in the dissipation in the iso-PIT results. However, the gain by the production is higher in
655 the aniso-PIT results, which overcompensates the extra loss by the anisotropic model. This explains
656 the slightly larger fluctuation obtained using the anisotropic PIT model than that using the isotropic
657 one.

658

659 4 SUMMARY AND CONCLUSIONS

660 This work is dedicated to a comprehensive validation of the set of closure models [assembled](#) in Shi
661 and Rzehak (2020), which comprise expressions for the interfacial forces including the drag, lift,
662 and turbulent dispersion. Based on the Euler-Euler / RANS approach, these closure models were
663 applied to predict the solid-liquid two-phase flows in a standard stirred tank reactor. To assess the
664 performance of the set of closure models, the predictions were compared with a recent experiment
665 by Sommer et al. (2021), in which spatially resolved data for the solid velocity and volume fraction
666 as well as liquid velocity and turbulence were provided. The comparison concerned 14 different
667 cases with variation in particle size, particle-to-liquid density ratio, mean solid volume fraction,
668 and impeller rotation speed. It turns out that by and large the experimental data were reasonably
669 well reproduced. However, the measurements show a small but clear effect of modulation of the
670 liquid phase turbulence by the particles, which could not be captured by the simulations even with
671 the aid of several particle-induced turbulence (PIT) models taken from the available literature.

672 Based on the present work and the previous ones from Shi and Rzehak (2018, 2020), several aspects
673 that deserve further consideration can be identified as follows. First, the overestimation of the peak
674 radial velocity in the single-phase case (Figure 1 and Figure 2, see also Fig. 6 in Sommer et al.
675 2021) by the SSG RSM model is a bit surprising, as very good agreement was obtained at
676 comparable impeller Reynolds number in our previous work (Figs. 8 & 9 in Shi and Rzehak 2018,
677 Fig. 4 in Shi and Rzehak 2020). The key difference among these cases lies in the magnitude of the
678 typical shear rate. In the present work a very high impeller rotation speed (1500 rpm) was
679 considered, making the typical shear rate involved much larger than those in the previous work. A
680 possible reason relates to the no-slip boundary condition applied at the edge of the impeller, as
681 there are evidences for the slip of Newtonian liquids at solid interfaces at high shear rates (Neto et
682 al. 2005).

683 Second, an appropriate PIT model reproducing the turbulence modulation in solid-liquid stirred
684 tank flows is still missing. In particular, neither the enhanced-eddy-viscosity model by Sato et al.
685 (1981) nor the two source-term based models originating from Kataoka et al. (1992) were found
686 capable to reproduce the turbulence enhancement revealed by the experiment in the case PE-dpS-
687 vofL. For future model development, the most promising candidate is likely the latter approach, as
688 it allows to directly modify the turbulent kinetic energy (or Reynolds stress) and the dissipation
689 using appropriate source terms. [The still open question here is the lack of general expressions that
690 are capable of accurately describing the variation in these source terms over a broad range of
691 parameters.](#)

692 [Furthermore, the mismatch between the predicted turbulence modulation using the source-term
693 based PIT models and the experimental data deserves some further discussion.](#) The source for the
694 turbulent kinetic energy is always treated as proportional to the work by the drag. In the present
695 work, the magnitude of the PIT source following this estimation was found always vanishingly

696 small, owing to the small slip velocity (therefore small slip Reynolds number). Therefore, we
697 expect that new proposals for the source term in the dissipation equation have to be established and
698 assessed. More specifically, in the present work the source for turbulence dissipation is treated as
699 proportional to the drag coefficient [first part of Eq. (10)] which depends on the slip Reynolds
700 number only. This treatment is certainly not general since other aspects, like e.g. the finite-size
701 effects (Yeo et al. 2010) and the effects of particle inertia (Ferrante and Elghobashi 2003), which
702 are known to be responsible for the modulation of the dissipation over a certain range of parameters,
703 are not accounted for. In this context, it seems promising to propose a more general expression by
704 relating the dissipation source with the particle momentum number (Tanaka and Eaton 2008).

705 Moreover, the choice for the timescale relating the two distinct source terms has to be revisited.
706 The reasonability of the timescale used in the present work, $\tau = d_p/u_{rel}$, has been justified only
707 for flows with large slip Reynolds numbers [$Re_p = O(100)$, Ma et al. (2017)]. A key feature of
708 such flows is that the turbulence modulation is largely governed by the wake dynamics. For flows
709 with low-to-moderate Re_p as considered in the present work, the wake is weak and there is no
710 guarantee that the same choice for the timescale still applies. Further assessment using other
711 possible timescale candidates (Rzehak and Krepper 2013) may be necessary. Recent DNS studies
712 on turbulence modulation (e.g. Yu et al. 2021, Xia et al. 2021) may provide a sufficient data source
713 to make progress in this direction.

714 Third, knowledge on the required mesh resolution is insufficient. Prior work addressing this
715 numerical issue mainly concerned the flow in the single-phase case (e.g. Coroneo et al. 2011, Lane
716 2017), while the requirement of a relatively higher mesh resolution in the corresponding two-phase
717 cases is revealed comparing the preliminary results reported in this work and those in Sommer et
718 al. (2021). This is particularly important in obtaining mesh independent results for the particle
719 distribution. The present work indicated that higher mesh resolution is required in cases with larger
720 particle size, larger particle density, and smaller impeller rotation speed. Whether these are general
721 trends needs further check.

722 Finally yet importantly, the development of reliable CFD models should be accompanied by the
723 acquisition of more accurate and more comprehensive data for validation. Further experimental
724 data and highly-resolved simulation results on wider operational conditions would be desirable
725 such as higher solid fraction, partially suspended conditions and maybe some more challenging
726 situations with polydisperse particles and non-standard tank geometries.

727 **5 ACKNOWLEDGEMENT**

728 This project has received funding from the European Union’s Horizon 2020 research and
729 innovation program FineFuture under Grant Agreement No 821265. Computational resources were
730 provided by HZDR.

731

732 **6 REFERENCES**

733 Balachandar, S. and Eaton, J.K., 2010. Turbulent dispersed multiphase flow. *Annual Review of*
734 *Fluid Mechanics* 42, 111–133.

- 735 Bujalski, W., Nienow, A., Chatwin, S., Cooke, M., 1986. The dependency on scale and material
736 thickness of power number of different impeller types. *Proceedings of the International*
737 *Conference on Mechanical Agitation*, p. 37.
- 738 Chapple, D., Kresta, S.M., Wall, A. and Afacan, A., 2002. The effect of impeller and tank geometry
739 on power number for a pitched blade turbine. *Chemical Engineering Research and Design* 80, 364–
740 372.
- 741 Chen, Y., Jiang, H. and Huang, X., 2011. Turbulence Properties of Solid-liquid Flow in the Near
742 Wall Region of Stirred Tank. *Journal of Chemical Engineering of Japan* 44, 224–232.
- 743 Colombo, M. and Fairweather, M., 2015. Multiphase turbulence in bubbly flows: RANS
744 simulations. *International Journal of Multiphase Flow* 77, 222–243.
- 745 Coroneo, M., Montante, G., Paglianti, A. and Magelli, F., 2011. CFD prediction of fluid flow and
746 mixing in stirred tanks: Numerical issues about the RANS simulations. *Computers & Chemical*
747 *Engineering* 35, 1959–1968.
- 748 Lopez de Bertodano, M.A.L., 1998. Two fluid model for two-phase turbulent jets. *Nuclear*
749 *Engineering and Design* 179, 65–74.
- 750 Deen, N.G., Solberg, T. and Hjertager, B.H., 2002. Flow generated by an aerated Rushton impeller:
751 two-phase PIV experiments and numerical simulations. *The Canadian Journal of Chemical*
752 *Engineering* 80, 1–15.
- 753 Derksen, J.J., 2003. Numerical simulation of solids suspension in a stirred tank. *AIChE Journal* 49,
754 2700–2714.
- 755 Derksen, J.J., 2018. Eulerian-Lagrangian simulations of settling and agitated dense solid-liquid
756 suspensions—achieving grid convergence. *AIChE Journal* 64, 1147–1158.
- 757 Drew, D.A. and Passman, S.L., 2006. Theory of multicomponent fluids. *Springer Science &*
758 *Business Media*.
- 759 Druzhinin, O.A. and Elghobashi, S., 1999. On the decay rate of isotropic turbulence laden with
760 microparticles. *Physics of Fluids* 11, 602–610.
- 761 Eaton, J.K., 2009. Two-way coupled turbulence simulations of gas-particle flows using point-
762 particle tracking. *International Journal of Multiphase Flow* 35, 792–800.
- 763 Eaton, J.K. and Fessler, J., 1994. Preferential concentration of particles by turbulence. *International*
764 *Journal of Multiphase Flow* 20, 169–209.
- 765 Elghobashi, S., 2006. An updated classification map of particle-laden turbulent flows. *In IUTAM*
766 *Symposium on Computational Approaches to Multiphase Flow*, 3–10. Springer, Dordrecht.
- 767 Elghobashi, S. and Truesdell, G., 1993. On the two - way interaction between homogeneous
768 turbulence and dispersed solid particles. I: Turbulence modification. *Physics of Fluids A: Fluid*
769 *Dynamics* 5, 1790–1801.
- 770 Feng, X., Li, X., Cheng, J., Yang, C. and Mao, Z.S., 2012. Numerical simulation of solid–liquid
771 turbulent flow in a stirred tank with a two-phase explicit algebraic stress model. *Chemical*
772 *Engineering Science* 82, 272–284.

773 Ferrante, A. and Elghobashi, S., 2003. On the physical mechanisms of two-way coupling in
774 particle-laden isotropic turbulence. *Physics of Fluids*, 15, 315–329.

775 Gabriele, A., Tsoligkas, A.N., Kings, I.N. and Simmons, M.J.H., 2011. Use of PIV to measure
776 turbulence modulation in a high throughput stirred vessel with the addition of high Stokes number
777 particles for both up-and down-pumping configurations. *Chemical Engineering Science* 66, 5862–
778 5874.

779 Gai, G., Hadjadj, A., Kudriakov, S. and Thomine, O., 2020. Particles-induced turbulence: A critical
780 review of physical concepts, numerical modelings and experimental investigations. *Theoretical
781 and Applied Mechanics Letters* 10, 241–248.

782 Geiss, S., Dreizler, A., Stojanovic, Z., Chrigui, M., Sadiki, A. and Janicka, J., 2004. Investigation
783 of turbulence modification in a non-reactive two-phase flow. *Experiments in Fluids* 36, 344–354.

784 Gillissen, J.J.J. and Van den Akker, H.E.A., 2012. Direct numerical simulation of the turbulent
785 flow in a baffled tank driven by a Rushton turbine. *AIChE Journal* 58, 3878–3890.

786 Guha, D., Ramachandran, P.A., Dudukovic, M.P. and Derksen, J.J., 2008. Evaluation of large Eddy
787 simulation and Euler-Euler CFD models for solids flow dynamics in a stirred tank reactor. *AIChE
788 Journal* 54, 766–778.

789 Gore, R.A. and Crowe, C.T., 1989. Effect of particle size on modulating turbulent intensity.
790 *International Journal of Multiphase Flow* 15, 279–285.

791 Hetsroni, G., 1989. Particles-turbulence interaction. *International Journal of Multiphase Flow* 15,
792 735–746.

793 Hoque, M.M., Mitra, S., Sathe, M.J., Joshi, J.B. and Evans, G.M., 2016. Experimental investigation
794 on modulation of homogeneous and isotropic turbulence in the presence of single particle using
795 time-resolved PIV. *Chemical Engineering Science* 153, 308–329.

796 Hosokawa, S. and Tomiyama, A., 2004. Turbulence modification in gas–liquid and solid–liquid
797 dispersed two-phase pipe flows. *International Journal of Heat and Fluid Flow* 25, 489–498.

798 Kataoka, I., Besnard, D.C. and Serizawa, A., 1992. Basic equation of turbulence and modeling of
799 interfacial transfer terms in gas-liquid two-phase flow. *Chemical Engineering Communications*
800 118, 221–236.

801 Kim, S.D. and Kang, Y., 1997. Heat and mass transfer in three-phase fluidized-bed reactors—an
802 overview. *Chemical Engineering Science* 52, 3639–3660.

803 Lane, G.L., 2017. Improving the accuracy of CFD predictions of turbulence in a tank stirred by a
804 hydrofoil impeller. *Chemical Engineering Science* 169, 188–211.

805 Li, G., Li, Z., Gao, Z., Wang, J., Bao, Y. and Derksen, J.J., 2018. Particle image velocimetry
806 experiments and direct numerical simulations of solids suspension in transitional stirred tank flow.
807 *Chemical Engineering Science* 191, 288–299.

808 Lu, J., Peters, E.A.J.F. and Kuipers, J.A.M., 2019. Direct numerical simulation of fluid flow and
809 dependently coupled heat and mass transfer in fluid-particle systems. *Chemical Engineering
810 Science* 204, 203–219.

811 Ma, T., Santarelli, C., Ziegenhein, T., Lucas, D. and Fröhlich, J., 2017. Direct numerical
812 simulation-based Reynolds-averaged closure for bubble-induced turbulence. *Physical Review*
813 *Fluids* 2, 034301.

814 Ma, T., Lucas, D., Jakirlić, S., and Fröhlich, J., 2020. Progress in the second-moment closure for
815 bubbly flow based on direct numerical simulation data. *Journal of Fluid Mechanics* 883, A9.

816 Mathai, V., Lohse, D. and Sun, C., 2020. Bubbly and buoyant particle-laden turbulent flows.
817 *Annual Review of Condensed Matter Physics* 11, 529–559.

818 Mesa, D. and Brito-Parada, P.R., 2019. Scale-up in froth flotation: A state-of-the-art review.
819 *Separation and Purification Technology* 210, 950–962.

820 Meyer, D.W., 2012. Modelling of turbulence modulation in particle-or droplet-laden flows.
821 *Journal of Fluid Mechanics* 706, 251–273.

822 Mishra, P. and Ein-Mozaffari, F., 2020. Critical review of different aspects of liquid-solid mixing
823 operations. *Reviews in Chemical Engineering* 36, 555–592.

824 Montante, G., Paglianti, A. and Magelli, F., 2012. Analysis of dilute solid-liquid suspensions in
825 turbulent stirred tanks. *Chemical Engineering Research and Design* 90, 1448–1456.

826 Murthy, B.N., Kasundra, R.B. and Joshi, J.B., 2008. Hollow self-inducing impellers for gas-liquid-
827 solid dispersion: Experimental and computational study. *Chemical Engineering Journal* 141, 332–
828 345.

829 Neto, C., Evans, D.R., Bonaccorso, E., Butt, H.J. and Craig, V.S., 2005. Boundary slip in
830 Newtonian liquids: a review of experimental studies. *Reports on Progress in Physics* 68, 2859.

831 Nouri, J.M. and Whitelaw, J.H., 1992. Particle velocity characteristics of dilute to moderately dense
832 suspension flows in stirred reactors. *International Journal of Multiphase Flow* 18, 21–33.

833 Ochieng, A. and Onyango, M.S., 2008. Drag models, solids concentration and velocity distribution
834 in a stirred tank. *Powder Technology* 181, 1–8.

835 Parekh, J. and Rzehak, R., 2018. Euler-Euler multiphase CFD-simulation with full Reynolds stress
836 model and anisotropic bubble-induced turbulence. *International Journal of Multiphase Flow* 99,
837 231–245.

838 Poelma, C., Westerweel, J. and Ooms, G., 2007. Particle-fluid interactions in grid-generated
839 turbulence. *Journal of Fluid Mechanics* 589, 315–351.

840 Qi, N., Zhang, H., Zhang, K., Xu, G. and Yang, Y., 2013. CFD simulation of particle suspension
841 in a stirred tank. *Particuology* 11, 317–326.

842 Risso, F., Roig, V., Amoura, Z., Riboux, G. and Billet, A.M., 2008. Wake attenuation in large
843 Reynolds number dispersed two-phase flows. *Philosophical Transactions of the Royal Society A:*
844 *Mathematical, Physical and Engineering Sciences* 366, 2177–2190.

845 Rushton, J.H., Costich, E.W. and Everett, H.J., 1950. Power characteristic of mixing impellers.
846 Part II. *Chemical Engineering Progress* 46, 457–476.

847 Rutherford, K., Mahmoudi, S.M., Lee, K.C. and Yianneskis, M., 1996. The influence of Rushton
848 impeller blade and disk thickness on the mixing characteristics of stirred vessels. *Chemical*
849 *Engineering Research & Design* 74, 369–378.

850 Rzehak, R. and Krepper, E., 2013. CFD modeling of bubble-induced turbulence. *International*
851 *Journal of Multiphase Flow* 55, 138–155.

852 Santarelli, C. and Fröhlich, J., 2015. Direct numerical simulations of spherical bubbles in vertical
853 turbulent channel flow. *International Journal of Multiphase Flow* 75, 174–193.

854 Santarelli, C. and Fröhlich, J., 2016. Direct numerical simulations of spherical bubbles in vertical
855 turbulent channel flow. Influence of bubble size and bidispersity. *International Journal of*
856 *Multiphase Flow* 81, 27–45.

857 Sato, Y., Sadatomi, M. and Sekoguchi, K., 1981. Momentum and heat transfer in two-phase bubble
858 flow—I. Theory. *International Journal of Multiphase Flow* 7, 167–177.

859 Schiller, L. and Naumann, A., 1933. Fundamental calculations in gravitational processing.
860 *Zeitschrift Des Vereines Deutscher Ingenieure* 77, 318–320.

861 Schwarz, M.P., Koh, P.T.L., Wu, J., Nguyen, B. and Zhu, Y., 2019. Modelling and measurement
862 of multi-phase hydrodynamics in the Outotec flotation cell. *Minerals Engineering* 144, 106033.

863 Shan, X., Yu, G., Yang, C., Mao, Z.S. and Zhang, W., 2008. Numerical simulation of liquid– solid
864 flow in an unbaffled stirred tank with a pitched-blade turbine downflow. *Industrial & Engineering*
865 *Chemistry Research* 47, 2926–2940.

866 Shi, P. and Rzehak, R., 2018. Bubbly flow in stirred tanks: Euler-Euler/RANS modeling. *Chemical*
867 *Engineering Science* 190, 419–435.

868 Shi, P. and Rzehak, R., 2019. Lift Forces on Solid Spherical Particles in Unbounded Flows.
869 *Chemical Engineering Science* 208, 115145.

870 Shi, P. and Rzehak, R., 2020. Solid-liquid flow in stirred tanks: Euler-Euler/RANS modeling.
871 *Chemical Engineering Science* 227, 115875.

872 Sommer, A.E., Rox, H., Shi, P., Eckert, K. and Rzehak, R., 2021. Solid-liquid flow in stirred
873 tanks:“CFD-grade” experimental investigation. *Chemical Engineering Science* 245, 116743.

874 Speziale, C. G., Sarkar, S. and Gatski, T. B., 1991. Modeling the pressure–strain correlation of
875 turbulence: an invariant dynamical systems approach, *Journal of Fluid Mechanics* 227, 245–272.

876 Tamburini, A., Cipollina, A., Micale, G. and Brucato, A., 2013. Particle distribution in dilute solid
877 liquid unbaffled tanks via a novel laser sheet and image analysis based technique. *Chemical*
878 *Engineering Science* 87, 341–358.

879 Tanaka, T. and Eaton, J.K., 2008. Classification of turbulence modification by dispersed spheres
880 using a novel dimensionless number. *Physical Review Letters* 101, 114502.

881 Unadkat, H., Rielly, C.D., Hargrave, G.K. and Nagy, Z.K., 2009. Application of fluorescent PIV
882 and digital image analysis to measure turbulence properties of solid–liquid stirred suspensions.
883 *Chemical Engineering Research and Design* 87, 573–586.

884 Wang, F., Wang, W., Wang, Y. and Mao, Z., 2003. CFD simulation of solid-liquid two-phase flow
885 in baffled stirred vessels with Rushton impellers. *Proceedings of the 3rd International Conference*
886 *on CFD in the Minerals and Process Industries*, 287–292.

887 Wu, J., Wang, S., Nguyen, B., Lane, G., Graham, L., Short, G. and Rüster, J., 2015. Improved
888 viscous slurry agitation for minerals processing. *Minerals Engineering* 78, 21–31.

- 889 Xia, Y., Lin, Z., Pan, D. and Yu, Z., 2021. Turbulence modulation by finite-size heavy particles in
890 a downward turbulent channel flow. *Physics of Fluids* 33, 063321.
- 891 Yeo, K., Dong, S., Climent, E. and Maxey, M.R., 2010. Modulation of homogeneous turbulence
892 seeded with finite size bubbles or particles. *International Journal of Multiphase Flow* 36, 221–233.
- 893 Yu, Z., Xia, Y., Guo, Y. and Lin, J., 2021. Modulation of turbulence intensity by heavy finite-size
894 particles in upward channel flow. *Journal of Fluid Mechanics* 913.
- 895